ACCEPTED MANUSCRIPT

Comparison of the diagenetic and reservoir quality evolution between the anticline crest and flank of an Upper Jurassic carbonate gas reservoir, Abu Dhabi, United Arab Emirates

Daniel Morad[a, *], Fadi H. Nader[b], Marta Gasparrini[b], Sadoon Morad[c], Carlos Rossi[d], Elisabetta Marchionda[e], Fatima Al Darmaki[f], Marco Martines[f] and Helge Hellevang[a]

[a]Department of Geosciences, University of Oslo, Pb 1047 Blindern, 0316, Oslo, Norway
[b]IFP Energies nouvelles, 92852 Rueil-Malmaison, France
[c]Department of Petroleum Geosciences, The Petroleum Institute, Khalifa University of Science and Technology, P.O. Box 2533, Abu Dhabi, United Arab Emirates
[d]Departmento de Petrología y Geoquímica, Universidad Complutense, 28040 Madrid, Spain
[e]Department of Earth and Environmental Sciences, University of Pavia, 27100, Pavia, Italy
[f] ADNOC Sour Gas, P.O. Box: 44115, Abu Dhabi, United Arab Emirates

ABSTRACT

This petrographic, stable isotopic and fluid inclusion microthermometric study of the Upper Jurassic limestones of an onshore field, Abu Dhabi, United Arab Emirates (UAE) compares diagenesis in flanks and crest of the anticline. The results revealed that the diagenetic and related reservoir quality

* Corresponding author
E-mail address: d.j.morad@geo.uio.no (D.Morad)

ACCEPTED MANUSCRIPT

evolution occurred during three phases, including: (i) eogenesis to mesogenesis 1, during which reservoir quality across the field was either deteriorated or preserved by calcite cementation presumably derived from marine or evolved marine pore waters. Improvement of reservoir quality was due to the formation of micropores by micritization of allochems and creation of moldic/intragranular pores by dissolution of peloids and skeletal fragments. (ii) Obduction of Oman ophiolites and formation of the anticline of the studied field was accompanied by cementation by saddle dolomite and blocky calcite. High homogenization temperatures (125–175°C) and high salinity (19–26 wt% NaCl eq) of the fluid inclusions, negative $\delta^{18}O_{VPDB}$ values (–7.7 to –2.9‰), saddle shape of dolomite, and the presence of exotic cements (i.e. fluorite and sphalerite) suggest that these carbonates were formed by flux of hot basinal brines, probably related to this tectonic compression event. (iii) Mesogenesis 2 during subsidence subsequent to the obduction event, which resulted in extensive stylolitization and cementation by calcite. This calcite cement occluded most of the remaining moldic and inter-/intragranular pores of the flank limestones (water zone) whereas porosity was preserved in the crest. This study contributes to: (1) our understanding of differences in the impact of diagenesis on reservoir quality evolution in flanks and crests of anticlines, i.e. impact of hydrocarbon

ACCEPTED MANUSCRIPT

emplacement on diagenesis, and (2) relating various diagenetic processes to burial history and tectonic events of foreland basins in the Arabian Gulf area and elsewhere.

Keywords: Diagenesis, carbonate, reservoir quality, fluid evolution, foreland basins

ACCEPTED MANUSCRIPT

ACCEPTED MANUSCRIPT

1. Introduction

Carbonate reservoirs are commonly heterogeneous owing to rapid changes in depositional facies and to the effects of various diagenetic processes (Sarg, 1988; Schroeder, 1988; Major and Holtz, 1990; Booler and Tucker, 2002; Morad et al., 2012a). Diagenetic processes may destroy, create or preserve porosity and permeability in carbonate reservoirs. These processes are controlled by multiple parameters that include primary mineralogy of the sediment, pore-water composition, burial-thermal history of the basin and hydrocarbon emplacement (e.g. Longman, 1980; Feazel and Schatzinger, 1985; Scholle and Halley 1985; Mazzullo and Harris, 1992; Ehrenberg et al., 2012; Morad et al., 2012b; Nader et al., 2013).

Despite voluminous publications on the diagenesis of carbonate deposits, published research work based on systematic comparisons of the distribution and impact of various diagenetic processes on reservoir quality evolution between the crest and the flanks of oil and gas fields are scarce. The commonly reported better reservoir quality in the crests than flanks has been attributed to the retardation of diagenesis by hydrocarbon emplacement (e.g. Feazel and Schatzinger, 1985; Oswald et al., 1995; Ehrenberg et al., 2016; Morad et al., 2016; Paganoni et al., 2016).

This study of Upper Jurassic Arab Formation D

ACCEPTED MANUSCRIPT

Member in a sour gas field onshore Abu Dhabi, United Arab Emirates (Fig. 1) employs integrated petrography, stable carbon, oxygen, strontium and sulfur isotopes, and microthermometry of fluid inclusions to compare the distribution and conditions of diagenetic processes and their impact on reservoir quality evolution in the crest and flanks of an anticline. The results obtained will thus also shed light on: (i) the impact of gas emplacement on burial diagenesis, and (ii) the origin and geochemical evolution of pore waters during near-surface conditions, burial phases and the tectonic evolution of the basin. The definitions of the diagenetic stages (i.e. eogenesis and mesogenesis) are adopted from Choquette and Pray (1970).

Cores from dolomite and anhydrite beds (i.e. Arab A, B and C members) were only available in the crest wells in this study. These beds and associated dolomitization processes will hence be excluded from this study.

2. Geological setting

2.1. Overview of the Arab Formation

Abu Dhabi is situated in the NE part of the Arabian Plate, bounded in the NW by the Qatar Arch and in the E and NE by the Oman Mountains (Alsharhan, 1989). The studied

ACCEPTED MANUSCRIPT

field is located SW of Abu Dhabi (Fig. 1 A, B). During the Jurassic, the Arabian Plate was located around 10–15°S, facing the Tethys Ocean (Handford et al., 2002). Carbonates and evaporites prevailed across the Arabian Gulf during the Jurassic (Sharland et al., 2001; Ziegler, 2001).

The Upper Jurassic (Kimmeridgian to Tithonian) Arab Formation comprises a thick succession of carbonates and intercalated evaporites (Fig. 2; Alsharhan and Whittle, 1995). The Arab Formation includes four members, which are named from bottom to top Arab D, C, B and A (Fig. 2; e.g. Alsharhan, 1989). The overlying evaporite-dominated Hith Formation is the main seal in the area (Fig. 2; Alsharhan and Scott, 2000).

Since the Late Jurassic, the development of two fold-and-thrust belts has affected the Abu Dhabi basin: (1) the obduction of the Oman ophiolites (Late Cretaceous), which resulted in the emplacement of oceanic sediments onto the eastern margin of the Arabian Platform (Searle et al., 1988) and (2) the Zagros Orogeny (Late Eocene/Oligocene to present), which resulted from the collision of the Arabian and Eurasian plates and the concomitant closure of the Neo-Tethys Ocean (Stampfli and Borel, 2002; Agard et al., 2011). The formation of the anticline in the studied field took mainly place during early Late Cretaceous through Middle Eocene.

The studied field (Fig. 1C) consists of a gently dipping, elongated anticline, which belongs to a series of structural traps

ACCEPTED MANUSCRIPT

that are characterized by NE–SW alignment of fold axes. The NE–SW trend seems to be associated with the thrusting that occurred in Oman when the Zagros Mountains were folded (Alsharhan and Scott, 2000). The measured bottom hole temperatures in the crest and flank are around 140°C and 160°C, respectively, indicating that the present day geothermal gradient is around 38°C/km.

There are two possible source rocks for the Upper Jurassic to Lower Cretaceous reservoirs in the UAE (Alsharhan and Scott, 2000): (i) the Diyab Formation (early Late Jurassic), which reached the phase of maximum oil generation in onshore areas of Abu Dhabi during the Early Eocene. (ii) The organic-rich Hanifa Formation (early Upper Jurassic), which entered the oil generation window during Middle Cretaceous (Ayoub and En Nadi, 2000).

2.2. Sedimentology of the Arab D Member

Limestones of the lower Arab D Member are dominated by dark grey, bioturbated massive mudstones and wackestones that are intercalated with floatstones that are rich in skeletal fragments (bivalves and gastropods), foraminifera, algae and mud intraclasts (Marchionda et al., 2018). The mudstones and wackestones are interpreted to have deposited in an outer ramp environment and the floatstones are interpreted as storm events

ACCEPTED MANUSCRIPT

(Marchionda et al., 2018). The floatstones are characterized by an erosive base and by the presence of inner ramp transported allochems. The transition between outer ramp and shoal is represented by mid-ramp deposits, defined by similar facies encountered in the outer ramp, but dominated by wackestones and the presence of local packstones. The upper Arab D is composed dominantly of cross/parallel laminated or massive grainstones and packstones (Marchionda et al., 2018). The allochems in the limestones include mainly ooids, peloids, and bioclasts (echinoderm, bivalve fragments and foraminifera). Deposition of these limestones is suggested to have occurred in shoal and mid ramp environments (Marchionda et al., 2018). Moreover, an exposure surface has been recognized on top of the upper Arab D (Lawrence et al., 2015). For a more detailed depositional and sequence stratigraphic framework of the studied field the reader is referred to Lawrence et al. (2015), Hollis et al. (2017) and Marchionda et al. (2018).

3. Samples and analytical methods

240 samples were collected from four wells. Three of the wells are located on the crest (wells A, B and C) and one on the flank (well D) of the anticline (Fig. 1C). Thin sections were prepared for all samples after vacuum impregnation with blue epoxy. Petrographic analyses were performed on the thin

ACCEPTED MANUSCRIPT

sections after staining them with alizarin red S and potassium ferricyanide in order to distinguish dolomite and calcite and their iron content (Dickson, 1966). The thin sections were examined by conventional, cathodoluminescence (CL), fluorescence (UV-light), and backscattered electron (SEM-BSE) microscopy. The CL analyses were conducted using a Technosyn Cold CL (Model 8200 Mark II, Technosyn Corp., Cambridge, MA, USA) and an OPEA system (OPEAFrance). Operative conditions were 10–15 kV gun potential, 300–500 μA beam current, 0.05 Torrvacuum, and 5 mm beam width. JMicroVision (Roduit, 2005) was used for point counting 500 points (random grid) on fifty-seven selected scanned thin sections in order to get quantitative information of the abundance of various cements and porosity. Representative small sample chips covered with gold-palladium and carbon coated thin sections were examined by a scanning electron microscope (SEM; FEI Quanta 200 with an acceleration voltage of 30kV) equipped with an Energy Dispersive X-ray Spectrometer.

For oxygen, carbon, sulfur, and strontium isotope analyses micro-samples were obtained from polished rock slabs using a dental drill and a micro-mill (computer-automated) mounted on binocular microscopes. Carbon and oxygen isotopes were obtained for eighty-nine calcite and nine dolomite samples. For the purpose of oxygen and carbon

ACCEPTED MANUSCRIPT

isotope analyses of calcite and dolomite, samples were reacted with 100% phosphoric acid at 25ºC and 50ºC for four hours, respectively. The evolved CO_2 gas was analyzed for isotopic ratios using a Delta-plus mass spectrometer (University of Windsor, Canada). The phosphoric acid fractionation factors for calcite at 25ºC and 50ºC for dolomite were applied (cf. Al-Aasm, et al, 1990). The isotopic data are reported in per mil (‰) relative to the V-PDB standard. The precision of carbon and oxygen isotope values is better than 0.05‰. Sulfur isotope ratios were analyzed for twenty-six samples and the $\delta^{34}S$ values are reported in ‰ relative to CDT. Solid samples were analyzed for sulfur on a Costech Elemental Analyzer (CHNS-O ECS 4010-Italy) coupled to an Isochrom Continuous Flow Stable Isotope Ratio Mass Spectrometer (GVI/Micromass-UK, 1995; University of Waterloo, Canada). Sulfate samples are corrected by using $BaSO_4$ standards NBS-127, EIL-42 and EIL-41 ($PbSO_4$). The error for such clean $BaSO_4$ standard material is ± 0.3‰ for sulfur. The ratios of $^{87}Sr/^{86}Sr$ isotopes were obtained for four calcite, three dolomite and three sulfate samples by using an automated Finnigan 261 mass spectrometer equipped with nine Faraday collectors (Ruhr-Universität Bochum, Germany). Correction for isotopic fractionation during the analyses was made by normalization to $^{86}Sr/^{88}Sr = 0.1194$. The mean standard error of mass spectrometer performance was ± 0.00003 for standard NBS-

ACCEPTED MANUSCRIPT

987.

Petrographic analyses of the fluid inclusions were carried out on eleven unstained wafers prepared without inducing substantial sample heating. The study focused on primary and pseudosecondary fluid inclusions belonging to petrographically consistent fluid inclusion assemblages, typically isolated or in crystal cores. Fluid inclusion microthermometry were performed on a Linkam MDS 600 heating-freezing stage (IFPEN, France), calibrated with synthetic fluid inclusions (H_2O, H_2O-NaCl and CO_2). The stage is mounted on a Nikon LV100 Eclipse, with 100 W mercury vapor lamp that allowed UV-light observations. Linksys 32 software was used to run the operations for microthermometric analyses. In aqueous inclusions, the homogenization temperatures (T_h) and final ice melting temperatures (T_{mice}) were measured in all samples, and the apparent eutectic temperature (T_e), i.e. the upper constraint of real eutectic temperature as determined from visual observation of the first melt, was reported where possible. The accuracy during microthermometric measurements was mostly ± 2.5°C for T_h and ± 0.2°C for T_{mice}. The total salinity, expressed as wt% NaCl eq., was calculated from T_{mice} by using the Bodnar (1993) equation. In order to avoid reequilibration of the fluid inclusions, heating runs were performed before freezing runs (Goldstein and Reynolds, 1994). For inclusions containing

ACCEPTED MANUSCRIPT

other gases than vapor, the gas in solution is known not to have significant impact on the homogenization temperature estimations (Roedder and Kopp, 1975). No pressure correction was applied to the measured homogenization temperatures (T_h); therefore they have to be considered as minimum trapping temperatures.

Porosity data were obtained for 882 core plugs (diameter of 3.8 cm) from the four studied wells. Prior to measurements, the core plugs were examined for microfractures, cleaned by oil extractor and dried in a vacuum oven at 60ºC for 24 hours. A helium porosimeter was used for porosity measurements.

4. Results

4.1. Petrography of the limestones

The diagenetic phases and events in the studied carbonate succession, which include micritization and dissolution of allochems (dominantly ooids), cementation by calcite and saddle dolomite, mechanical and chemical compaction and cementation by minor non-carbonate phases, occur both in the crest and flank of the anticline. However, the abundance of some of these phases and events varies between the crest and flank wells. The three crest wells display similar

ACCEPTED MANUSCRIPT

abundance of the various diagenetic phases and events. The below outlined diagenetic phases and events are described within the constrained paragenetic order.

The ooids and skeletal fragments display nil to complete micritization (i.e. the formation of peloids; Fig. 3). Micritization of the outermost part of these allochems has resulted in the formation of thin micrite envelopes (5–10 μm wide). Completely micritized allochems (Fig. 3A–C, E, G), which contain various amounts of microporosity, are common in the grainstones in the crest (i.e. shoal facies). Visual estimations indicate that micritized allochems in the flank contain far less microporosity (i.e. more cemented) than the crest (Fig. 4). The micritized ooids are well rounded and, typically around 200 to 400 μm in size, and lack or have vague concentric internal fabric (Fig 3A). The non-micritized ooids, which display radial internal fabric, have similar shapes and size range as the micritized ones (Fig. 3D, F, H). SEM examinations of micritized allochems show that the micrite has anhedral, spheroidal (rounded), subhedral and euhedral shapes (e.g. Morad et al., 2016), and is 1 to 4 μm wide (Fig. 4).

Brown dull-luminescent dogtooth/scalenohedral shaped circumgranular calcite rims (here refered to as C1; 5–20 μm in size) occur around many micritized and non-micritized allochems in packstones and grainstones in the upper Arab D Member. These calcite rims comprise less than 3% of the

ACCEPTED MANUSCRIPT

cement in packstones and grainstones and are equally common in the crest and flank.

Ooids and skeletal fragments in packstones and grainstones are, in some cases, partly or completely dissolved resulting in the formation of moldic and enlarged inter-/intragranular pores (Figs. 3A, D, G). Such pores are found in packstones, grainstones (upper Arab D Member) and, less commonly, in floatstones (lower Arab D Member) across the anticline. These types of pores are either empty, or filled partly to completely by calcite cements in the crest (Fig. 3D, G), while they are completely cemented in the flank of the anticline (Figs. 3E, 6B).

Fine to medium sized (5–200 μm wide) equant calcite crystals (here refered to as C2) occur as cement in inter-/intragranular and moldic pores (Fig. 3) in the upper Arab D Member and in fractures (Fig. 6F) in the lower Arab D Member. This calcite cement phase is dull orange under CL (Fig. 5) and engulfs the circumgranular calcite rims. Drusy equant calcite cement (here refered to as C3; > 100–2000 μm wide) occurs in moldic and inter-/intragranular pores (Fig. 6B) and is characterized by alternating dull orange to bright yellow luminescence (Fig. 5B). The fine to medium equant and drusy equant calcite cements account together for around 15 to 50% of the volume in grainstones (upper Arab D Member) being more abundant in the flank (av. 35%) than in the crest (av.

ACCEPTED MANUSCRIPT

27%) of the anticline (Table 1). Syntaxial calcite overgrowths (1 to 7%; here refered to as C4; up to 1000 μm) occur around echinoderm fragments in packstones and grainstones (Fig. 6A) in the upper Arab D Member. The intergranular volume is greater between grains that are engulfed by syntaxial calcite compared to grains lacking cementation (Fig. 6A). Syntaxial calcite, which typically exhibits dull orange to dull yellow concentric zones under CL, occurs in similar amounts in crest (av. 3%) and flank (av. 3.5%; Table 1).

Packstones and grainstones with small amounts of circumgranular rims, fine to medium equant and syntaxial calcite contain allochems that have point and tangential contacts (Fig 3D, F, H). No significant difference has been noticed in the extent of mechanical compaction in packstones and grainstones between the crest and flanks of the anticline.

Minor amounts of scattered framboidal pyrite (< 1%), sphalerite (< 1%) and quartz cements (Figs. 6B; up to 4 %) occur in the crest and flank. Small amounts of medium- to coarse-crystalline (up to 120 μm wide) dolomite rhombs (planar-e crystals) occur along and in the vicinity of wispy seams and stylolites.

Anhydrite nodules and blocky/poikilotopic anhydrite and celestine have replaced host limestones (Fig. 6C) and skeletal fragments. These sulfates are, in general, not crosscut by stylolites. These sulfates are relatively abundant (0–25%) in

ACCEPTED MANUSCRIPT

some of the floatstones in the lower Arab D Member in the crest, whereas rare in grainstones (0–2%; shoal facies) in the upper Arab D Member. Only trace amounts of sulfates were observed in the flank (< 1 %). The sulfate nodules and cements are, in some cases, completely to partly replaced by fine to blocky calcite. Calcitized anhydrite is more common in the flank well than in the crest wells (Fig 6C vs. 6D).

Fluorite crystals (300–1000 μm wide; up to 1%) occur mainly along stylolites and fill fractures and vugs in mudstones and wackestones in the lower Arab D in the flank. Fluorite is commonly associated with and engulfed by saddle dolomite and blocky calcite. Small (1–10 μm wide) discrete pyrite crystals have replaced sulfates, quartz, blocky calcite and saddle dolomite cements in both crest and flank.

Bright red luminescent saddle dolomite crystals (Fig. 5 B, D; up to 2 mm wide; up to 15%), which exhibit the typical sweeping extinction and curved faces, occur as cement in fractures, vugs and along stylolites (Fig. 6D, F, H). Saddle dolomite is mainly present in the lower Arab D Member where it has also replaced the nodular and blocky anhydrite, and skeletal fragments in wackestones and floatstones (Fig 6G). Saddle dolomite is equally common in the crest and flank (around 6%; Table 1), except along stylolites where it is more abundant in the flank.

ACCEPTED MANUSCRIPT

Dull orange to dull yellow luminescent blocky calcite (here refered to as C5; 200–2000 μm; 0–25%) occurs in moldic pores mainly in floatstones (lower Arab D) and along stylolites (Fig. 6H) and fractures. The blocky calcite, which is the last calcite cement observed, has replaced saddle dolomite and sulfate cements (Fig. 6D, H). This calcite phase is more common in the flank (19%) than crest (13%; Table 1), particularly as an anhydrite-replacing phase and along stylolites.

Stylolites (Fig. 6E, F, H) as well as dissolution, wispy seams and sutured intergranular contacts are common in the studied limestones. Stylolites have amplitudes of millimeters to centimeters and are more common in mudstones and wackestones (lower Arab D Member) than in packstones and grainstones (upper Arab D Member). The stylolites are typically bedding-parallel whereas stylolites that are vertical or oblique to bedding are rare and have low amplitude. Stylolites have, in general, higher amplitude and are more frequent in the flank than in the crest (Table 1). The amplitude and abundance of stylolites is particularly higher in the packstones and grainstones in the flank than in the crest. The dissolution surfaces in the packstones/grainstones in the crest are mainly wispy seams (i.e. low amplitude surfaces). Visual estimations indicate that carbonate cements (saddle dolomite and blocky calcite; Fig. 6F, H) are more common along the stylolites in the

ACCEPTED MANUSCRIPT

flank than those in the crest (Fig. 6E). Vertical to subvertical fractures with variable size (10–1500 μm wide) are more common in mudstones and wackestones than in packstones and grainstones. These fractures are either open or partly/completely filled by fine to blocky calcite cement. Most of the fractures are aligned perpendicular to the stylolites (Fig. 6F). Visual estimations indicate that fractures are more abundant in the flank than crest.

4.2. Porosity and permeability

Modal analysis of macroporosity in thirty-seven representative thin sections of grainstones revealed that porosity ranges between nil and 11% (av. 3.5%) in the crest and is nil in the flank (Table 1). Intergranular (up to 10%) and moldic/intragranular pores (up to 3%) are the most common macropore types. Macropores were not observed in grainstones in the flank well.

The micritized ooids in packstones and grainstones have variable amounts of micropores (< 10–20 μm; Lønøy, 2006) between the micrite particles and, less commonly, macropores (> 20–30 μm). Open to partly cemented microfractures are occasionally observed in the mudstones and wackestones. The measurement of volumes of micropores is difficult because they are very thin (μm to nm; Fig. 4; Morad et al., 2016) and

ACCEPTED MANUSCRIPT

any eventual chemical variation between the overgrowth and micrite cores is below the magnification limits of the CL and backscattered electron imaging.

Average core-plug porosity values in packstones and grainstones are around 15% higher in the crest than in the flank of the anticline. Average core-plug porosity values in mudstones and wackestones are around 5% higher in the crest than in the flank of the anticline.

4.3. Isotope geochemistry

The isotope data for the various micro-drilled carbonate and sulfate phases in the Arab Formation are displayed in Figures 7 and 8, and in Table 1. Blocky calcite (C5) in vugs and molds has $\delta^{18}O_{VPDB}$ values from –6.5 to –4.1‰ (av. –5.3‰) and $\delta^{13}C_{VPDB}$ values from +0.6 to +2.1‰ (av. +1.5‰). Blocky calcite in crest samples shows $\delta^{18}O_{VPDB}$ values from –6.5 to –4.7‰ (av. –6.0‰) and $\delta^{13}C_{VPDB}$ values from +1.1 to +2.0‰ (av. +1.7‰). Blocky calcite samples from the flank well show higher $\delta^{18}O_{VPDB}$ values (–5.0 to –4.1‰; av. –4.6‰) and similar $\delta^{13}C_{VPDB}$ values (+0.6 to +2.1‰; av. +1.5‰) compared to the crest. Two blocky calcite samples from the flank display $^{87}Sr/^{86}Sr$ ratios of 0.70698 and 0.70710 (av. 0.70704).

ACCEPTED MANUSCRIPT

The syntaxial calcite overgrowths (C4; analyzed only in the crest) have $\delta^{18}O_{VPDB}$ values ranging from –7.2 to –5.2‰ (av. –6.2‰) and $\delta^{13}C_{VPDB}$ values from –1.2 to +1.7‰ (av. +0.5‰). Bulk limestone samples display $\delta^{18}O$ values from –6.6 to –2.9‰ (av.–4.9‰) and $\delta^{13}C$ values from –3.0 to +3.6‰ (av. +1.9‰). Bulk limestone samples have similar O and C isotopic composition in the crest and flank of the anticline. There is no significant difference in oxygen isotope composition between the different limestone textures, hence there is no significant difference between the upper and lower Arab D Member (Table 1). The $\delta^{13}C_{VPDB}$ values are slightly higher in the mudstones/wackestones (lower Arab D) than grainstones and packstones (upper Arab D; Table 1). Two bulk limestone samples display $^{87}Sr/^{86}Sr$ ratios between 0.70694 (mudstone) and 0.70696 (grainstone), respectively.

The saddle dolomite samples in moldic pores and vugs have a wide range of $\delta^{18}O_{VPDB}$ values ranging from –7.7 to –2.9‰ (av. –4.6‰) and $\delta^{13}C_{VPDB}$ from +0.4 to +3.6‰ (av.+2.1‰). Saddle dolomite in samples from the crest shows $\delta^{18}O_{VPDB}$ values ranging from –7.7 to –3.7‰ (av. –5.7‰) and $\delta^{13}C_{VPDB}$ from +0.4 to +2.0‰(av. +1.2‰). Saddle dolomite in the flank well shows higher $\delta^{18}O_{VPDB}$ (–4.2 to –2.9‰; av. –3.6‰), and higher $\delta^{13}C_{VPDB}$ (+1.9 to +3.6‰; av. +2.8‰) values than in the crest. Saddle dolomite shows $^{87}Sr/^{86}Sr$ ratios between 0.70693 and 0.70701 (av. 0.70697).

ACCEPTED MANUSCRIPT

The anhydrite and celestine cements have $\delta^{34}S_{CDT}$ values ranging from +23.1 to +24.7‰ (av. +23.8‰) and $^{87}Sr/^{86}Sr$ ratios between 0.70693 and 0.70701 (av. 0.70696) in the crest. Due to the low abundance we were not able to analyze sulfate cements in the flank well.

4.4. Fluid inclusion petrography and microthermometry

Petrography of celestine and fine to medium equant (C2), drusy (C3), syntaxial (C4) and blocky (C5) calcite cements, and saddle dolomite cements in the investigated rock samples revealed the presence of aqueous primary and pseudosecondary fluid inclusions. Fluorescence due to the presence of oil was only observed in secondary fluid inclusions along microfractures in one sample.

Fine to medium equant calcite (C2) is characterized by irregular, rounded and rectangular (2-10 μm) fluid inclusions with varying liquid-vapor ratios (5–15% vapor), including all-liquid inclusions. The fluid inclusions occur in clusters and are typically located close to the framework grains, suggesting that the inclusions were trapped relatively early. Syntaxial calcite (C4) cements are characterized by relatively small (1–6 μm) and irregular shaped fluid inclusions that occur isolated or in clusters. Both all-liquid and two-phase fluid inclusions with varying liquid-vapor ratios (5–15% vapor) were observed. The

ACCEPTED MANUSCRIPT

fluid inclusions observed in drusy calcite (C3) cements occur isolated or along growth zones and they have irregular, rounded and rectangular shapes (2-10 μm). Both all-liquid and two-phase fluid inclusions with relatively consistent liquid-vapor ratios (10–15% vapor) were observed. Blocky calcite (C5) is characterized by relatively large and irregular two-phase (10–15% gas) inclusions (5–20 μm) that are distributed as isolated or grouped in clusters (Fig. 9A, B). Poikilotopic celestine cement in the outer ramp facies (crest well) is characterized by small (2–5 μm) rounded to irregular, all-liquid and two-phase, primary fluid inclusions with relatively consistent liquid-vapor ratios (5–10% vapor). Saddle dolomite cements are characterized by the presence of inclusion-rich cores and inclusion-poor rims (Fig. 9C, D). Focus was put on rectangular (negative crystal) and irregular inclusion in the crystal cores because of their primary origin (Goldstein and Reynolds, 1994). Fluid inclusions in the saddle dolomite are two-phase and typically small (1–5 μm) with a gas phase occupying around 10–15% of the inclusions.

Total homogenization occurred in the liquid phase for all analyzed inclusions. All analyzed inclusions froze during the first cooling run. The fluid inclusions in drusy calcite in a crest well displayed one phase-change at around –90°C, which was evident by a sudden movement of the vapor bubble. Final melting temperature of ice in the fluid inclusions in the crest

ACCEPTED MANUSCRIPT

(i.e. calcite with drusy texture) occurred under metastable conditions ($T_{miceMET}$); i.e. abrupt melting at temperatures above the true T_{mice}. Fluid inclusions in saddle dolomite and blocky calcite (in the flank well) display at least two phase-changes during the first cooling run. First, a contraction of the vapor bubble occurs, which is possibly induced by the formation of clathrates (Vandeginste et al., 2009). With further cooling, ice and salt hydrates (ice-like phases) nucleated to give completely frozen fluid inclusions. In blocky calcite, the nucleation of clathrates and ice-like phases occurred at around –50°C and –75°C, respectively, whereas this occurred at about –58 and –84°C in saddle dolomite cements.

The T_h data of fine to medium equant calcite (C2) in the flank fall in the range 55–130°C (mode of 90°C; Fig. 10A). Suitable fluid inclusions for microthermometry analyses were not observed in this calcite phase from the crest. In drusy calcite (C3) in the crest, the T_h data fall in the range 65–125°C (mode of 95°C; Fig. 10B). $T_{miceMET}$ occurred between –27.2 and –26.6°C. The total salinity calculated from $T_{miceMET}$ falls in the range 26.3–26.9 wt% NaCl eq and underestimates true salinity. Suitable fluid inclusions for microthermometry analyses were not observed in the drusy calcite from the flank. In syntaxial calcite (C4) cements, the T_h data fall in the range 80–125°C (mode of 110°C; Fig. 10C). The T_h is similar in the crest (80–125°C) and flank (80–120°C). The T_h in some of the

ACCEPTED MANUSCRIPT

fluid inclusion assemblages in equant, syntaxial and drusy calcite cements are relatively inconsistent (i.e. varies more than 10–15°C; Goldstein and Reynolds, 1994). Moreover, in fine to medium equant calcite, syntaxial calcite and celestine the small size of the fluid inclusions hindered low-temperature measurements. In celestine cement in the crest, the T_h data (Fig. 10D) fall in the relatively narrow range 100–120°C (mode of 110°C).

The T_h of blocky calcite (C5) fall in the range 115–150°C (mode of 145°C; Fig. 10E). The T_h of blocky calcite in the flank is, overall, higher (115–160°C) than in the crest (120–130°C). The T_{mice} ranges between –24.4 and –17.8°C (modes of –18 and –23°C) and the salinity values fall in the range 19.2–25.2 wt% NaCl eq (Fig. 10G; modes of 21.0 and 24.5 wt% NaCl eq). Apparent eutectic temperatures in these fluid inclusions range from around –58 to –50°C. Low-temperature measurements of blocky calcite were only measured in the flank.

The T_h and salinity data of inclusion rich cores of saddle dolomite crystals (Fig. 10F, G) range from 140 to 175°C (mode of 160°C) and 25.6 to 26.3 wt% NaCl eq (mode of 26.0 wt% NaCl eq), respectively. The T_{mice} values range between –26.2 and –25.0°C (mode –26°C). The small size of the inclusions made it difficult to obtain the salinity values in most of the saddle dolomite hence we only have salinity data from the

ACCEPTED MANUSCRIPT

flank well. The T_h data of saddle dolomite in crest samples are slightly lower (140 to 160°C; mode 155°C) than flank samples (145 to 175°C; mode 160°C). Apparent eutectic temperatures in saddle dolomite fluid inclusions from the flank were recorded from –46 to –36°C. During reheating, the dissociation of clathrates occurred between +5 and +25°C in both the blocky calcite and saddle dolomite.

5. Discussion

The petrographic, isotopic and fluid inclusion analyses, coupled with the burial-tectonic history (Fig. 11) of the basin have allowed constraining the history of diagenetic (Fig. 12) and related reservoir quality evolution across the anticline prior to, during and subsequent to gas migration and emplacement.

5.1. Micritization of allochems

The mechanism, timing and diagenetic environment of micritization are controversial (Budd, 1989; Moshier, 1989a; Reid and Macintyre, 2000; Léonide et al., 2014; Hollis et al., 2017). Micritization of ooids and skeletal fragments has been suggested to occur by micro-boring organisms (e.g. endolithic bacteria, algae and fungi) at and immediately below the seafloor (e.g. Bathurst, 1966; Longman, 1980; James and

ACCEPTED MANUSCRIPT

Choquette, 1984), by recrystallization on the seafloor (Reid and Macintyre, 2000) or by microbially mediated nanoglobule formation and subsequent merging into larger crystals (Tucker and Marshall, 2004). Micritization of allochems, which ultimately results in the formation of peloids, in the upper Arab D Member is interpreted to have occurred in marine waters. The rapid deposition of ooid-rich grainstones does not preclude extensive micritization of the ooids because microbial activities are expected to be common not only at but also below the seafloor (Loucks and Budd, 1981; Melzer and Budd, 2008; Okubo et al., 2015). The presence of spheroidal micrite in the peloids has been used by Reid and Macintyre (2000) and Morad et al. (2016) to argue that micritization occurrs by microbes that bored into allochems causing their dissolution and simultaneous micrite precipitation. A pre-compactional origin for micritization is supported by high total intergranular volume of grainstones that are rich in micritized allochems (cf. Geslin, 1994). The seafloor eogenetic timing (Choquette and Pray, 1970) accounts for the equal extent of micritization of allochems between the crest and flank samples of the studied field.

The considerably lower $\delta^{13}C_{VPDB}$ values (–3.0‰ and –1.5‰) of non-micritized ooid-rich grainstones at the top of the shoal facies than grainstones with severely to completely micritized ooids (av. $\delta^{13}C_{VPDB}$ = +1.9‰) indicate that the

ACCEPTED MANUSCRIPT

cementation by calcite was influenced by incursion of meteoric waters during subaerial exposure. The $\delta^{13}C_{VPDB}$ values for the former grainstones are lower than those of Late Jurassic seawater ($\delta^{13}C_{VPDB}$ = –0.1 to +2.5‰; Veizer et al., 1999). The presence of a surface of subaerial exposure in the studied field has been inferred by Lawrence et al. (2015) and Hollis et al. (2017).

Our results suggest that micritization of allochems has resulted in:

(i) The formation and/or increase of micropores between micrite particles (Loucks and Budd, 1981; Moshier, 1989b; Al-Aasm and Azmy, 1996; Fischer et al., 2014), which altered the porosity in packstones and grainstones from dominantly macropores to bimodal micro- and macropore distribution.

(ii) Increase in the water-rock interaction because the relatively small micrite particles have larger surface area/volume ratio compared to non-micritized allochems. Thus the micritized allochems were presumably subjected to dissolution according to the Ostwald ripening phenomena (Morse and Casey, 1988; Volery et al., 2010). Difficulties in providing evidence for dissolution of micrites (e.g. presence of pits) is attributed to the precipitation of ultra thin (<

ACCEPTED MANUSCRIPT

1 μm) calcite micro-overgrowths around them (Morad et al., 2016). These overgrowths can thus explain the common euhedral shape of the micrites particularly in the flank limestones, which have been cemented more extensively by such overgrowths than the crest.

(iii) More ductile properties of the limestones (cf. Regnet et al., 2015), which would increase the susceptibility of packstones and grainstones to porosity and permeability loss by mechanical compaction. However, dissolution of micritzed grains and reprecipitation as equant and syntaxial calcite have supported the framework of the limestones and thus prevented more extensive mechanical compaction. This postulation is supported by more compacted grainstones that have low peloid contents (Fig. 3D, F).

Hollis et al. (2017) suggested an alternative mechanism for the micritization (alteration) of allochems in the Arab Formation and hence also the formation of intragranular microporosity. These authors suggested that the allochems (mainly ooids) were originally aragonitic and that microporosity in the peloids was formed due to dissolution of aragonite crystals and reprecipitation as microcrystalline calcite crystals. However, the conversion of aragonite to calcite, which

ACCEPTED MANUSCRIPT

is a neomorphic process, is known to occur pseudomorphically, i.e. the shapes of aragonite crystals are preserved; no textural evidence (e.g. needle-like or fibrous crystal shapes) supporting aragonite precursors were observed in this study. The fabric destructive mechanism proposed by Hollis et al. (2017) would contradict the use of pseudomorphic conversion of aragonite into calcite, which makes the basis for the important and widely accepted and used inference of calcite versus aragonite seas (Sandberg, 1983). Moreover, we are unaware of any reports of chemical conversion of aragonitic allochems into micrite. Instead, as it is the case in this study, aragonite skeletal fragments tend to dissolve and the resulting moldic pores are often filled by equant (often drusy) calcite cements. Thus, the latter features can be just considered as a normal cementation event, i.e. the moldic pores behaved like any other pores, such as intergranular pores.

5.2. Dissolution of allochems

The original mineralogy of the allochems provides important clues to the origin of intragranular/moldic pores and the paleoclimatic conditions (Saller and Moore, 1989). The presence of secondary pores owing to dissolution of aragonitic allochems is often attributed to fluxes of meteoric waters below surfaces of subaerial exposures (e.g. Choquette and Pray, 1970;

ACCEPTED MANUSCRIPT

James and Choquette, 1984). Nevertheless, it has been argued that aragonitic allochems can also dissolve in marine pore waters (Saller and Moore, 1989; Melim et al., 1995; Munnecke et al., 1997). This postulation, combined with the unlikely significant flux of meteoric waters in the arid paleoclimate, suggest that the formation of moldic pores by dissolution of aragonitic skeletal fragments (i.e. many of the bivalves and gastropods) in the Jurassic limestones occurred during marine pore water diagenesis. This process can, however, not explain dissolution of the ooids because the global atmospheric and seawater composition during the Late Jurassic favored precipitation of calcitic ooids (Sandberg, 1983). Thus, the consistent pervasive dissolution of micritized ooids and micritized calcitic skeletal fragments compared to non-micritized calcitic allochems paves the road for an alternative mechanism of formation of moldic and intragranular pores in limestones. As suggested above the micritization of calcitic allochems promotes water-rock reaction because micrite has higher surface area/volume ratio compared to the unaltered allochems. Consequently, dissolution of micritized allochems can obey the Ostwald ripening theory (Morse and Casey, 1988; Volery et al., 2010) as discussed above. The dissolved mass is interpreted to have been redistributed in the host limestones as more stable fine to medium equant (C2), drusy (C3) and syntaxial (C4) calcite cements. Evidence supporting this

ACCEPTED MANUSCRIPT

interpretation include: (i) lack of dissolution features (typically etched surfaces) in these calcite cements; (ii) presence of remnants of minor micrite in the moldic and intragranular pores (Fig. 3G); and (iii) more abundant calcite cements in grainstones containing dissolved micritized allochems than in grainstones with non-micritized allochems. The presence of moldic and secondary intragranular pores formed by dissolution of micritized allochems in calcite-cemented grainstones with large total intergranular volume indicates that dissolution started during eogenesis prior to significant burial.

5.3. Origin of calcite cements

The various sizes, distribution patterns, paragenetic relationships with other minerals, indicate that calcite cements have likely various origins and formation conditions. The crystal shape and lack of luminescence of the circumgranular calcite rims (C1) around allochems suggests precipitation in the near-surface marine phreatic realm (e.g. James and Jones, 2016). An early eogenetic origin of this calcite cement explains its equal abundance in packstones and grainstones (upper Arab D Member) of the crest and flank wells.

The paragenetic relationships, similar CL characteristics and ranges of T_h data of fine to medium equant calcite (55–130°C; C2), drusy calcite (65–125°C; C3) and syntaxial calcite

ACCEPTED MANUSCRIPT

(80–125°C; C4) cements suggest that they are derived from the same cement generation. The wide ranges of T_h data and the presence of all-liquid fluid inclusions (i.e. indicate temperatures < 50°C; Goldstein and Reynolds, 1994) within these calcite cements suggest: (i) continuous precipitation during burial; (ii) that the fluid inclusions were thermally reequilibrated during recrystallization at various temperatures; or (iii) that recrystallization occurred at relatively low temperature and the inclusions were later reset during burial heating. However, most T_h values are between 80 and 110ºC, which suggest that the possible recrystallization event and/or further cementation may have occurred within this temperature range. Recrystallization is supported by the presence of all-liquid together with two-phase fluid inclusions, inconsistent liquid-vapor ratios and the relatively wide range of T_h data in some of the analyzed fluid inclusion assemblages (Goldstein and Reynolds, 1994). Moreover, the high intergranular volume of allochems engulfed by these calcite cements suggests that at least some of these cements started to precipitate before significant mechanical compaction. However, even small amounts of scattered calcite cement could have resulted in preservation of porosity (Morad et al., 2012b). Hence, such pores can be cemented during later burial diagenesis.

The sources of these calcite cements with marine or evolved marine pore waters were possibly dissolution of

ACCEPTED MANUSCRIPT

peloids and dissolution of aragontic skeletal fragments in the shallower burial regime, and stylolitization in the deeper burial regime (Oswald et al., 1995; Neilson et al., 1998; Fabricius and Borre, 2007; Vandeginste and John, 2013; Paganoni et al., 2016), or both. The mass released from stylolitization would presumably diffuse and reprecipitate within a few meters away from stylolites (Ehrenberg et al., 2016). The onset of extensive stylolite development, and hence massive release of Ca^{2+} and HCO_3^- is difficult to constrain, but has been suggested to occur at greater depths than 1500 m in limestones (Paganoni et al., 2016; Ehrenberg et al., 2016). The microfractures that are aligned perpendicular to the stylolites were presumably formed during this time (Nelson, 1981; Ameen et al., 2010). It would be meaningless to constrain a mass balance of dissolved peloids versus precipitated calcite because: (i) cement is provided by both dissolution of calcite peloids and aragonitic skeletal fragments as well as stylolitization of the limestones; and (ii) it is difficult to quantify microporosity and ultra thin micro-overgrowths by modal analyses.

Shift in the chemistry of formation waters from Mg-rich to Ca-rich can be constrained by using T_{mice} and apparent eutectic temperatures of carbonate cements. The T_{mice} (–24.4 and –17.8°C) and apparent eutectic temperatures (–58 to –50°C) of fluid inclusions in blocky calcite (C5) indicate that the brines were highly saline (19.2–25.2 wt% NaCl eq) and

ACCEPTED MANUSCRIPT

contained other salts than NaCl, possibly $CaCl_2$ (Oakes et al., 1990, Goldstein and Reynolds, 1994). These results corroborate a shift from Mg-rich to Ca-rich brines. Thus, blocky calcite (C5), which post-dates saddle dolomite, might have formed owing to a shift in composition of the hot dolomitizing basinal brines. The typically lower T_h of these calcites (mode 145°C) compared to saddle dolomites (mode 160°C) indicates formation during cooling of the hot basinal brines. The $\delta^{13}C_{VPDB}$ values (+0.6 to +2.1‰) and $^{87}Sr/^{86}Sr$ ratios (0.70698 to 0.70710) of blocky calcite are similar to Late Jurassic seawater and host limestone, which suggests dissolution of host limestone as the source. Moreover, calcite cementation subsequent to the precipitation of saddle dolomite has been reported in several other hydrothermal systems (e.g. Qing and Mountjoy, 1992; Merino and Canals, 2011; Mansurbeg et al., 2016; Sirat et al., 2016).

Using the range of oxygen isotope composition (–6.5 to –4.1‰) and T_h (115–150°C) and the calcite-water oxygen isotope fractionation equation of Friedman and O´Neil (1977), it is inferred that the parent fluids from which blocky calcite in the flank precipitated from were geochemically evolved basinal brines with $\delta^{18}O_{SMOW}$ values of +8.6 to +14.0‰ (cf. Zeeh et al., 1995; Calvo et al., 2011; Dickson and Kenter, 2014). The calculated $\delta^{18}O_{SMOW}$ values are, overall, lower in the crest (+9.0 to +11.8‰) than in the flank (+10.2 to +14.0‰), which

ACCEPTED MANUSCRIPT

indicate that the basinal brines had different compositions or various states of geochemical evolution.

5.4. Origin of saddle dolomite

Fluid inclusion microthermometry (T_h = 140 to 175°C; T_e = –46 to –36°C; salinity = 25.6 to 26.3 wt% NaCl eq.) indicates that saddle dolomite was formed from hot, NaCl-$MgCl_2$-$CaCl_2$ basinal brines. The data obtained in this study does not allow precise determination of the origin and the migration distance of these brines. Moreover, saddle dolomite is often associated with flux of hot basinal fluids (Spötl and Pitman, 1998; Machel, 2004; Paganoni et al., 2016; Mansurbeg et al., 2016; Sirat et al., 2016). The flux of such brines may flow along faults and fractures during the obduction of Oman ophiolites (cf. Paganoni et al., 2016). The $^{87}Sr/^{86}Sr$ ratio (0.70693 to 0.70701) and $\delta^{13}C_{VPDB}$ (+0.4 to +3.6‰) signatures of saddle dolomite are similar to the values of the ambient Late Jurassic seawater ($^{87}Sr/^{86}Sr$ ratios = 0.70687 to 0.70720; $\delta^{13}C_{VPDB}$ = –0.1 to 2.5‰; Veizer et al., 1999), which suggest that dissolution of the host carbonates was the source for Sr and C (cf. Morad et al., 2010).

The parent fluids of the saddle dolomite can be further constrained by using the temperature-dependent oxygen isotope fractionation equation for dolomite-water (Land, 1983). By

ACCEPTED MANUSCRIPT

using T_h (140 to 175°C) and $\delta^{18}O_{VPDB}$ (–7.7 to –2.9‰), the calculated $\delta^{18}O_{SMOW}$ values for saddle dolomite ($\delta^{18}O_{SMOW}$ of +6.9 to +14.3‰) indicate geochemically evolved basinal brines (cf. Zeeh et al., 1995; Calvo et al., 2011; Dickson and Kenter, 2014). The inferred wide range of $\delta^{18}O_{SMOW}$ of these brines is not well understood but might indicate involvement of several brine sources with different states of geochemical evolution. The calculated $\delta^{18}O_{SMOW}$ values, which are, overall, lower in the crest (+6.6 to +12.4‰) than in the flank (+10.6 to +14.3‰), indicate that the basinal brines had different compositions or states of geochemical evolution. A possible reason for the difference in $\delta^{18}O_{SMOW}$ is discussed below.

5.5. Origin of sulfate cements

The T_h data of fluid inclusions in celestine of outer ramp facies revealed a mode temperature of around 110°C, which suggest formation during deep-burial diagenesis or flux of hot fluids to shallower depths. Moreover, the sulfate nodules and cements meet some of the criteria suggested by Machel and Burton (1991) for recognizing a burial from evaporative near-surface origin, including: (i) nodules occur within, or juxtaposed to, stylolites; (ii) nodules replace host rock, and they may cross cut the boundaries between host rock and stylolites; and (iii) the nodules do not occur in lagoonal or supratidal

ACCEPTED MANUSCRIPT

facies. Burial diagenetic dissolution of anhydrite nodules, beds and cements in Arab A–C are possible sources for these sulfate cements. The considerably higher $\delta^{34}S_{CDT}$ values (av. +23.8‰) of the burial diagenetic anhydrite and celestine than Late Jurassic seawater ($\delta^{34}S_{CDT}$ = +14.2 to +18‰; Kampschulte and Strauss, 2004) suggest that they reacted with dissolved residual sulfate in the bacterial (BSR) or thermochemical sulfate reduction zone (TSR; Pierre, 1985; Chow et al., 2000; Machel, 2013). The T_h data of celestine (100–120°C) corroborate the TSR zone because BSR is suggested to take place between 0–80°C (e.g. Machel, 2001) while TSR from 100 to 140°C. The precipitation of small amounts of framboidal pyrite was likely a by-product of the BSR (Machel, 2001).

The absence of burial diagenetic sulfates in the flank in the Arab D Member is attributed the consumption of anhydrite by TSR (Machel, 2001). The presence of small remnants of sulfates within calcite cements indicates that sulfates were present prior to TSR. However, there is no evidence of extensive calcitization of anhydrite and celestine in the Arab Formation, yet the studied field has up to 30% H_2S. The H_2S in the field has, therefore, presumably migrated from elsewhere (Nederlof et al., 2016), likely from the Permo-Triassic Khuff Formation, which undergoes extensive TSR (e.g. Worden et al., 2000). This interpretation further supports the flux of extraformational hot basinal brines into the Arab Formation.

ACCEPTED MANUSCRIPT

5.6. Comparison of reservoir quality evolution in crest versus flanks

The distribution of most diagenetic phases across the field was presumably similar before the development of the anticline and gas emplacement. The timing of gas emplacement is uncertain, but hydrocarbon migration has been suggested to occur during the obduction of Oman ophiolites for a nearby field (cf. Paganoni et al., 2016). Moreover, the presence of gas in fluid inclusions in saddle dolomite and blocky calcite cements supports the suggestion that gas migration occurred during the obduction event, because these cements are thought to be formed during and shortly after the obduction. Hollis et al. (2017) suggested that oil emplacement in the field occurred during the Late Cretaceous and that gas emplacement occurred later during Oligo-Miocene.

Many of the pre-anticline diagenetic processes had a considerable impact on reservoir quality, such as micritization of the ooids and skeletal fragments and the subsequent dissolution of these and concomitant reprecipitation of fine to medium equant calcite cements. Reservoir quality of limestones in the crest (i.e. gas zone) has evolved differently from those in the flank (i.e. the water zone) in the field (Fig. 13). The only striking diagenetic feature that accounts for the

ACCEPTED MANUSCRIPT

15% average higher porosity of packstones/grainstones in the crest than the flanks is the greater abundance and, particularly, the higher amplitudes of stylolite in the flank than crest. Hence, the better reservoir quality in the crest than the flank of the anticline is attributed to more calcite mass released during stylolitization in the flank. The lower amplitudes and lower amounts of stylolites in the crest are attributed to the retarding effect of gas emplacement on diagenesis (Feazel and Schatzinger, 1985; Oswald, 1995; Neilson et al., 1998; Heasley et al., 2000; Cox et al., 2010).

The type of calcite cement formed from the mass released during stylolitization is uncertain. The most significant difference in calcite cementation in grainstones between crest and flank is the more abundant micropore-filling and intergranular pore-filling equant calcite cement (C2) in the flank. Hence, this type of calcite is suggested to be sourced by stylolitization after gas emplacement in the crest. Moreover, the flank presumably contains only micropores because macropores are more readily cemented than micropores (Ehrenberg and Walderhaug et al., 2015; Deville De Periere et al., 2017).

Saddle dolomite and blocky calcite, which are interpreted to form by flux of hot basinal brines, have decreased the reservoir quality mainly in floatstones in the lower Arab D Member, but only marginally the packstones and

ACCEPTED MANUSCRIPT

grainstones in the upper Arab D Member. The presence of these cements mainly in the lower Arab D is uncertain, but could be because the basinal brines did not reach up to the upper Arab D through the low-permeability mudstones and wackestones, except along conduits such as fractures and stylolites.

The similar bulk $\delta^{18}O_{VPDB}$ values of the various limestones types in the crest and the flank are difficult to explain because we would expect more depleted $\delta^{18}O_{VPDB}$ values in the flank if calcite cementation continued here after gas emplacement. Possible explanations for this feature include: (i) calcite precipitation occurred mainly before and/or subsequent although at a slower rate in the crest after gas emplacement (Cox et al., 2010); and (ii) relatively small difference in depth and, thus, temperature between crest and flank (around 20°C higher in flank). Moreover, the similar bulk $\delta^{13}C_{VPDB}$ of limestones in crest and flank suggests a high degree of rock-buffering and that dissolution of the host carbonate sediments and connate marine pore waters were the main source for dissolved carbon (Morad et al., 2010). Additionally, lower $\delta^{18}O_{VPDB}$ values in saddle dolomite and blocky calcite in crest than in flank is enigmatic, because we would expect lower $\delta^{18}O_{VPDB}$ values in flank as they have precipitated at higher temperatures (Fig. 10E, D). However, $\delta^{18}O_{VPDB}$ values are not only controlled by the temperature, but also by the $\delta^{18}O_{SMOW}$ of

ACCEPTED MANUSCRIPT

the basinal brines (Epstein, 1959). The lower $\delta^{18}O_{VPDB}$ values in crest than in flank might, therefore, suggest that the flux of basinal brines controlled the $\delta^{18}O_{VPDB}$ values and not burial diagenesis.

6. Conclusions

This study helped constraining: (1) the timing and condition encountered during the diagenetic and reservoir quality evolution of the Upper Jurassic Arab Formation from a gas field onshore Abu Dhabi (UAE), and (2) the reasons for the main differences between the crest and flanks of the anticline. Important findings thus include:

- Before gas emplacement, important diagenetic alterations included micritization of allochems and formation of peloids with abundant microporosity followed by dissolution of these peloids, which sourced cementation by equant, drusy and syntaxial calcite cements.
- Diagenesis during the obduction of Oman ophiolite was presumably mediated by the expulsion of hot basinal brines, which resulted in the formation of saddle dolomite, blocky calcite and minor amounts of fluorite and sphalerite in the crest and flanks.

ACCEPTED MANUSCRIPT

ACCEPTED MANUSCRIPT

- Fluid inclusion microthermometry (T_h = 140–175°C; T_e apparent = –46 to –36°C; salinity = 25.6 to 26.3 wt% NaCl eq.) and oxygen isotope analyses ($\delta^{18}O_{VPDB}$ = –7.7‰ to –2.9‰) of saddle dolomite indicate precipitation from hot NaCl-$MgCl_2$-$CaCl_2$brines. The blocky calcite has replaced saddle dolomite and has lower T_h (115–150°C), which suggests formation during cooling of the hot brines.
- Deep-burial diagenesis, which occurred in the flanks during subsidence that followed the obduction of Oman ophiolites, resulted in extensive stylolitization and cementation by calcite cements. Conversely, stylolitization and calcite cementation were retarded in the crest owing to gas emplacement. Thus, calcite cementation related to stylolitization accounts for the far lower reservoir quality in the flanks compared to the crest.
- This study suggests that the diagenetic evolution pathways of limestones in foreland basins can be better understood when distinction is made between the role of intraformational fluids and flux of hot basinal brines.

Acknowledgments

The authors would like to thank the Petroleum Institute for funding this project (PIRC project number LTR14012) and ADNOC Sour Gas, ADNOC and Oxy for giving us access to samples, data and permission to publish the paper. We would

ACCEPTED MANUSCRIPT

also like to thank the Sedimentary Geology editor Dr. Brian Jones for handling of this manuscript and reviewers Dr. Cathy Hollis and Dr. Matthieu Deville de Periere for their valuable comments and suggestions.

ACCEPTED MANUSCRIPT

ACCEPTED MANUSCRIPT

References

Agard, P., Omrani, J., Jolivet, L., Whitechurch, H., Vrielynck, B., Spakman, W., Monie, P., Meyer, B., Wortel, R., 2011. Zagros orogeny: a subduction dominated process. Geological Magazine, 148, 692–725.

Al-Aasm, I. S., Azmy, K. K., 1996. Diagenesis and evolution of microporosity of middle-upper Devonian Kee Scarp Reefs, Norman wells, NWT, Canada: petrographic and chemical evidence. AAPG Bulletin, 80, 82–99.

Al-Aasm, I. S., Taylor, B. E., South, B., 1990. Stable isotope analysis of multiple carbonate samples using selective acid extraction. Chemical Geology: Isotope Geoscience Section, 80, 119–125.

Al Darmaki, F., Mattner, J., Bouzida, Y., Cavailhes, T., Burreson, M., Lawrence, D. A., Lucas, N. 2014. Identification, Upscaling and Modeling Strategy for Multi-Scale Fracture Networks in Variable Lithology Reservoirs. In EAGE Borehole Geology Workshop, 13–15 October, Dubai, UAE.

Alsharhan, A. S., 1989. Petroleum geology of the United Arab Emirates. Journal of Petroleum Geology, 123, 253–288.

Alsharhan, A. S., Scott, R. W., 2000. Hydrocarbon potential of Mesozoic carbonate platform-basin systems, UAE. Middle East models of Jurassic/Cretaceous Carbonate Systems. SEPM Special Publication 69, 335–358.

ACCEPTED MANUSCRIPT

Alsharhan, A. S., Whittle, G. L., 1995. Carbonate-evaporite sequences of the Late Jurassic, southern and southwestern Arabian Gulf. AAPG Bulletin, 79, 1608–1630.

Ameen, M. S., Buhidma, I. M., Rahim, Z., 2010. The function of fractures and in-situ stresses in the Khuff reservoir performance, onshore fields, Saudi Arabia. AAPG Bulletin, 94, 27–60.

Ayoub, M. R., En Nadi, I. M., 2000. Stratigraphic Framework and Reservoir Development of the Upper Jurassic in Abu Dhabi Onshore Area, UAE. SEPM Special Publication 69, 229–248.

Bathurst, R. G. C., 1966. Boring algae, micrite envelopes and lithification of molluscan biosparites. Geological Journal, 5, 15–32.

Bodnar, R. J., 1993. Revised equation and table for determining the freezing point depression of H_2O-NaCl solutions. Geochimica et Cosmochimica Acta, 57, 683–684.

Booler, J., Tucker, M. E., 2002. Distribution and geometry of facies and early diagenesis: the key to accommodation space variation and sequence stratigraphy: Upper Cretaceous Congost Carbonate platform, Spanish Pyrenees. Sedimentary Geology, 146, 225–247.

Budd, D. A., 1989. Micro-rhombic calcite and microporosity in limestones: A geochemical study of the lower cretaceous thamama group, UAE. Sedimentary Geology, 63, 293–311.

ACCEPTED MANUSCRIPT

Calvo, R., Ayalon, A., Bein, A., Sass, E., 2011. Chemical and isotopic composition of diagenetic carbonate cements and its relation to hydrocarbon accumulation in the Heletz-Kokhav oil field (Israel). Journal of Geochemical Exploration, 108, 88–98.

Choquette, P. W., Pray, L. C., 1970. Geologic nomenclature and classification of porosity in sedimentary carbonates. AAPG Bulletin, 54, 207–250.

Chow, N., Morad, S., Al-Aasm, I. S., 2000. Origin of authigenic Mn-Fe carbonates and pore-water evolution in marine sediments: evidence from Cenozoic strata of the Arctic Ocean and Norwegian-Greenland Sea (ODP Leg 151). Journal of Sedimentary Research, 70, 682–699.

Cox, P. A., Wood, R. A., Dickson, J. A. D., Al Rougha, H. B., Shebl, H., Corbett, P. W. M., 2010. Dynamics of cementation in response to oil charge: evidence from a Cretaceous carbonate field, UAE. Sedimentary Geology, 228, 246–254.

Deville De Periere, M. D., Durlet, C., Vennin, E., Caline, B., Boichard, R., Meyer, A., 2017. Influence of a major exposure surface on the development of microporous micritic limestones-Example of the Upper Mishrif Formation (Cenomanian) of the Middle East. Sedimentary Geology, 353, 96–113.

Dickson, J. A. D., 1966. Carbonate identification and genesis as revealed by staining. Journal of Sedimentary Research, 36, 107–118.

ACCEPTED MANUSCRIPT

Dickson, J. A. D., Kenter, J. A. M., 2014. Diagenetic evolution of selected parasequences across a carbonate platform: Late Paleozoic, Tengiz Reservoir, Kazakhstan. Journal of Sedimentary Research, 84, 664–693.

Ehrenberg, S. N., Walderhaug, O., 2015. Preferential calcite cementation of macropores in microporous limestones. Journal of Sedimentary Research, 85, 780–793.

Ehrenberg, S. N., Walderhaug, O., Bjorlykke, K., 2012. Carbonate porosity creation by mesogenetic dissolution: Reality or illusion?. AAPG Bulletin, 96, 217–233.

Ehrenberg, S. N., Morad, S., Yaxin, L., Chen, R., 2016. Stylolites and Porosity In A Lower Cretaceous Limestone Reservoir, Onshore Abu Dhabi, UAE. Journal of Sedimentary Research, 86, 1228–1247.

Epstein, S., 1959. Variations of 18O/16O ratio in nature and some geologic implications, Researches in Geochemistry Wiley, New York, 217–240.

Fabricius, I. L., Borre, M. K., 2007. Stylolites, porosity, depositional texture, and silicates in chalk facies sediments. Ontong Java Plateau–Gorm and Tyra fields, North Sea. Sedimentology, 54, 183–205.

Feazel, C. T., Schatzinger, R. A., 1985. Prevention of carbonate cementation in petroleum reservoirs. In: Schneiderman, N., Harris, P. M. (Eds.), Carbonate Cements. SEPM Special Publication, 36, 97–106.

ACCEPTED MANUSCRIPT

Fischer, C., Kurganskaya, I., Schäfer, T., Lüttge, A., 2014. Variability of crystal surface reactivity: What do we know?. Applied Geochemistry, 43, 132–157.

Friedman, I., O'Neil, J. R., 1977. Compilation of stable isotope fractionation factors of geochemical interest. Sixth ed. Data of Geochemistry 440, USGPO, pp. KK1–KK12.

Geslin, J. K., 1994. Carbonate pseudomatrix in siliciclastic-carbonate turbidites from the Oquirrh-Wood River Basin, southern Idaho. Journal of Sedimentary Research, 64, 55–58.

Goldstein, R. H., Reynolds, T. J., 1994. Systematics of fluid inclusions in diagenetic minerals: SEPM short course 31. Society for Sedimentary Geology, 199 pp.

Handford, C. R., Cantrell, D. L., Keith, T. H., 2002. Regional facies relationships and sequence stratigraphy of a supergiant reservoir (Arab-D member), Saudi Arabia. In Sequence-stratigraphic models for exploration and production: SEPM, Gulf Coast Section 22nd Annual Foundation Bob F. Perkins Research Conference, 539–563.

Heasley, E. C., Worden, R. H., Hendry, J. P., 2000. Cement distribution in a carbonate reservoir: recognition of a palaeo oil–water contact and its relationship to reservoir quality in the Humbly Grove field, onshore, UK. Marine and Petroleum Geology, 17, 639–654.

Hollis, C., Lawrence, D. A., de Perière, M. D., Al Darmaki, F., 2017. Controls on porosity preservation within a Jurassic

ACCEPTED MANUSCRIPT

oolitic reservoir complex, UAE. Marine and Petroleum Geology, 88, 888–906.

James, N. P., Choquette, P. W., 1984. Diagenesis 9. Limestones-the meteoric diagenetic environment. Geoscience Canada Reprint Series, 4, 45–78.

James. N., Jones, B., 2016. Origin of Carbonate Sedimentary Rocks. Wiley. United Kingdom (446 pp.).

Kampschulte, A., Strauss, H., 2004. The sulfur isotopic evolution of Phanerozoic seawater based on the analysis of structurally substituted sulfate in carbonates. Chemical Geology, 204, 255–286.

Land, L. S., 1983. The application of stable isotopes to studies of the origin of dolomite and to problems of diagenesis of clastic sediments: In: M.A. Arthur (Eds.) Stable Isotopes In Sedimentary Geology. Society of Economic Paleontologists and Mineralogists Short Course Note 10, 4.1–4.22.

Lawrence, D. A., Hollis, C., Green, D., de Perière, M. D., Al Darmaki, F., Bouzida, Y., 2015. Palaeogeographic Reconstruction of a Tide-Dominated Oolite Shoal Complex in the Lower Arab Formation, Onshore UAE. In Abu Dhabi International Petroleum Exhibition and Conference, 9–12 November, Abu Dhabi, UAE, SPE paper 172769–MS, 1–21.

Léonide, P., Fournier, F., Reijmer, J. J., Vonhof, H., Borgomano, J., Dijk, J., Rosenthal, M., van Goethem, M., Cochard, J., Meulenaars, K., 2014. Diagenetic patterns and pore space

ACCEPTED MANUSCRIPT

distribution along a platform to outer-shelf transect (Urgonian limestone, Barremian–Aptian, SE France). Sedimentary Geology, 306, 1–23.

Longman, M. W., 1980. Carbonate diagenetic textures from nearsurface diagenetic environments. AAPG Bulletin, 64, 461–487.

Loucks, R. G., Budd, D. A., 1981. Diagenesis and Reservoir Potential of the Upper Jurassic Smackover Formation of South Texas. Gulf Coast Association of Geological Societies, Transactions. 31, 339–446.

Lønøy, A., 2006. Making sense of carbonate pore systems. AAPG Bulletin, 90, 1381–1405.

Machel, H. G., 2001. Bacterial and thermochemical sulfate reduction in diagenetic settings—old and new insights. Sedimentary Geology, 140, 143–175.

Machel, H. G., 2004. Concepts and models of dolomitization: a critical reappraisal. In Braithwaite, C.J.R., Rizzi, C., Darke, G. (Eds.), The Geometry and Petrogenesis of Dolomite Hydrocarbon Reservoirs. Geological Society, London, Special Publications, 235, 7–63.

Machel, H. G., 2013. Secondary anhydrites in deeply buried Devonian carbonates of the Alberta Basin, Canada. Carbonates and Evaporites, 28, 267–280.

ACCEPTED MANUSCRIPT

Machel, H. G., Burton, E. A., 1991. Burial-diagenetic sabkha-like gypsum and anhydrite nodules. Journal of Sedimentary Research, 61, 394–405.

Major, R. P., Holtz, M. H., 1990. Depositionally and diagenetically controlled reservoir heterogeneity at Jordan field. Journal of Petroleum Technology, 42, 1–304.

Mansurbeg, H., Morad, D., Othman, R., Morad, S., Ceriani, A., Al-Aasm, I., Kolo, K., Spirov, P., Proust, J. N., Preat, A., Koyi, H., 2016. Hydrothermal dolomitization of the Bekhme formation (Upper Cretaceous), Zagros Basin, Kurdistan Region of Iraq: Record of oil migration and degradation. Sedimentary Geology, 341, 147–162.

Marchionda, E., Deschamps, R., Cobianchi, M., Nader, F. H., Di Giulio, A., Morad, D. J., Al Darmaki, F., Ceriani, A., 2018. Field-scale depositional evolution of the Upper Jurassic Arab Formation (onshore Abu Dhabi, UAE). Marine and Petroleum Geology, 89, 350–369.

Mazzullo, S. J., Harris, P. M., 1992. Mesogenetic dissolution: its role in porosity development in carbonate reservoirs. AAPG Bulletin, 76, 607–620.

Melim, L. A., Swart, P. K., Maliva, R. G., 1995. Meteoric-like fabrics forming in marine waters: Implications for the use of petrography to identify diagenetic environments. Geology, 23, 755–758.

ACCEPTED MANUSCRIPT

Melzer, S. E., Budd, D. A., 2008. Retention of high permeability during shallow burial (300 to 500 m) of carbonate grainstones. Journal of Sedimentary Research, 78, 548–561.

Merino, E., Canals, À., 2011. Self-accelerating dolomite-for-calcite replacement: Self-organized dynamics of burial dolomitization and associated mineralization. American Journal of Science, 311, 573–607.

Morad, D., Paganoni, M., Al Harthi, A., Morad, S., Ceriani, A., Mansurbeg, H., Al Suwaidi, A., Al-Aasm, I. S., Ehrenberg, S. N., 2016. Origin and evolution of microporosity in packstones and grainstones in a Lower Cretaceous carbonate reservoir, United Arab Emirates. In: Armitage, P. J., Butcher, A. R., Churchill, J. M., Csoma, A. E., Hollis, C., Lander, R. H., Omma, J. E., Worden, R. H. (Eds.), Reservoir Quality of Clastic and Carbonate Rocks: Analysis, Modelling and Predicition. Geological Society, London, Special Publications, 435, 435–20.

Morad, S., Al-Aasm, I. S., Sirat, M., Sattar, M. M., 2010. Vein calcite in cretaceous carbonate reservoirs of Abu Dhabi: Record of origin of fluids and diagenetic conditions. Journal of Geochemical Exploration, 106, 156–170.

Morad, S., Ketzer, J. M. M., De Ros, L. F., 2012a. Linking diagenesis to sequence stratigraphy: an integrated tool for understanding and predicting reservoir quality distribution. In: Morad, S., Ketzer, J. M. M., De Ros, L. F. (Eds.), Linking

ACCEPTED MANUSCRIPT

Diagenesis to Sequence Stratigraphy, International Association of Sedimentologists, Special Publication 45, 1–36.

Morad, S., Al-Aasm, I. S., Nader, F. H., Ceriani, A., Gasparrini, M., Mansurbeg, H., 2012b. Impact of diagenesis on the spatial and temporal distribution of reservoir quality in the Jurassic Arab D and C members, offshore Abu Dhabi oilfield, United Arab Emirates. GeoArabia, 17, 17–56.

Morse, J. W., Casey, W. H., 1988. Ostwald processes and mineral paragenesis in sediments. American Journal of Science, 288, 537–560.

Moshier, S. O., 1989a. Microporosity in micritic limestones: a review. Sedimentary Geology, 63, 191–213.

Moshier, S. O., 1989b. Development of microporosity in a micritic limestone reservoir, Lower Cretaceous, Middle East. Sedimentary Geology, 63, 217–240.

Munnecke, A., Westphal, H., Reijmer, J. J., Samtleben, C., 1997. Microspar development during early marine burial diagenesis: a comparison of Pliocene carbonates from the Bahamas with Silurian limestones from Gotland (Sweden). Sedimentology, 44, 977–990.

Nader, F. H., Boever, E., Gasparrini, M., Liberati, M., Dumont, C., Ceriani, A., Morad, S., Lerat, O., Doligez, B., 2013. Quantification of diagenesis impact on the reservoir properties of the Jurassic Arab D and C members (Offshore, UAE). Geofluids, 13, 204–220.

ACCEPTED MANUSCRIPT

Nederlof, P., Kaczorowski, N., Lawrence, D., 2016. The Origin of H_2S in the Arab Reservoirs in Abu Dhabi. In Abu Dhabi International Petroleum Exhibition and Conference, 7–10 November, Abu Dhabi, UAE, SPE paper 183336–MS, 1–10.

Neilson, J. E., Oxtoby, N. H., Simmons, M. D., Simpson, I. R., Fortunatova, N. K., 1998. The relationship between petroleum emplacement and carbonate reservoir quality: examples from Abu Dhabi and the Amu Darya Basin. Marine and Petroleum Geology, 15, 57–72.

Nelson, R. A., 1981. Significance of fracture sets associated with stylolite zones: geologic notes. AAPG Bulletin, 65, 2417–2425

Oakes, C. S., Bodnar, R. J., Simonson, J. M., 1990. The system NaCl-$CaCl_2$-H_2O: I. The ice liquidus at 1 atm total pressure. Geochimica et Cosmochimica Acta, 54, 603–610.

Okubo, J., Lykawka, R., Warren, L. V., Favoreto, J., Dias-Brito, D., 2015. Depositional, diagenetic and stratigraphic aspects of Macaé Group carbonates (Albian): example from an oilfield from Campos Basin. Brazilian Journal of Geology, 45, 243–258.

Oswald, E. J., Mueller III, H. W., Goff, D. F., Al-Habshi, H., Al-Matroushi, S., 1995. Controls on porosity evolution in Thamama Group carbonate reservoirs in Abu Dhabi, UAE. In Middle East Oil Show. Society of Petroleum Engineers, 15p.

Paganoni, M., Al Harthi, A., Morad, D., Morad, S., Ceriani, A., Mansurbeg, H., Al Suwaidi, A., Al-Aasm, I. S., Ehrenberg, S.

ACCEPTED MANUSCRIPT

N., Sirat, M., 2016. Impact of stylolitization on diagenesis of a Lower Cretaceous carbonate reservoir from a giant oilfield, Abu Dhabi, United Arab Emirates. Sedimentary Geology, 335, 70–92.

Pierre, C., 1985. Isotopic evidence for the dynamic redox cycle of dissolved sulphur compounds between free and interstitial solutions in marine salt pans. Chemical Geology, 53, 191–196.

Qing, H., Mountjoy, E. W., 1992. Large-scale fluid flow in the Middle Devonian Presqu'ile Barrier, Western Canada sedimentary basin. Geology, 20, 903–906.

Reid, R. P., Macintyre, I. G., 2000. Microboring versus recrystallization: Further insight into the micritization process: Current Ripples. Journal of Sedimentary Research, 70, 24–28.

Roduit, N., 2005. Two complementary efficient methods to quantify porosity types in digital images of thin sections with the software JmicroVision. In 24th IAS Meeting, Oman, abstracts, 142.

Regnet, J. B., David, C., Fortin, J., Robion, P., Makhloufi, Y., Collin, P. Y., 2015. Influence of microporosity distribution on the mechanical behavior of oolithic carbonate rocks. Geomechanics for Energy and the Environment, 3, 11–23.

Roedder, E., Kopp, O. C., 1975. A check on the validity of the pressure correction in inclusion geothermometry, using

ACCEPTED MANUSCRIPT

hydrothermally grown quartz. Fortschritte der Mineralogie, 52, 431–446.

Sandberg, P. A., 1983. An oscillating trend in Phanerozoic non-skeletal carbonate mineralogy. Nature, 305, 19–22.

Saller, A. H., Moore, C. H., 1989. Meteoric diagenesis, marine diagenesis, and microporosity in Pleistocene and Oligocene limestones, Enewetak Atoll, Marshall Islands. Sedimentary Geology, 63, 253–272.

Sarg, J. F., 1988. Carbonate sequence stratigraphy. In: Wilgus, C.K., Hastings, B.S., Kendall, C.G.St.C., Posamentier, H.W., Ross, C.A., van Wagoner, J.C. (Eds.) Sea-level Changes: an Integrated Approach. SEPM Special Publication 42, 155–181.

Scholle, P. A., Halley, R. B., 1985. Burial diagenesis: out of sight, out of mind! In: Schneiderman, N., Harris, P.M. (Eds.), Carbonate cements, SEPM Special Publication 36, 309–334.

Schroeder, J. H., 1988. Spatial variations in the porosity development of carbonate sediments and rocks. Facies, 18, 181–204.

Searle, M. P., 1988. Thrust tectonics of the Dibba zone and the structural evolution of the Arabian continental margin along the Musandam Mountains (Oman and United Arab Emirates). Journal of the Geological Society, 145, 43–53.

Sharland, P. R., Archer, R., Casey, D. M., Davies, R. B., Hall, S., Heward, A., Horbury, A., Simmons, M. D., 2004. Arabian plate

ACCEPTED MANUSCRIPT

sequence stratigraphy. GeoArabia, Special Publication 2. Gulf Petrolink, Bahrain. 371pp. and 3 enclosures.

Sirat, M., Al-Aasm, I. S., Morad, S., Aldahan, A., Al-Jallad, O., Ceriani, A., Morad, D., Mansurbeg, H., Al-Suwaidi, A., 2016. Saddle dolomite and calcite cements as records of fluid flow during basin evolution: Paleogene carbonates, United Arab Emirates. Marine and Petroleum Geology, 74, 71–91.

Spötl, C., Pitman, J. K., 1998. Saddle (baroque) dolomite in carbonates and sandstones: a reappraisal of the burial-diagenetic concept. In: Morad, S., (Eds.), Carbonate Cementation in Sandstones, International Association of Sedimentologists, Special Publication 26, 437–460.

Stampfli, G. M., Borel, G. D., 2002. A plate tectonic model for the Paleozoic and Mesozoic constrained by dynamic plate boundaries and restored synthetic oceanic isochrons. Earth and Planetary Science Letters, 196, 17–33.

Tucker, M., Marshall, J., 2004. Diagenesis and geochemistry of Upper Muschelkalk (Triassic) buildups and associated facies in Catalonia (NE Spain): a paper dedicated to Francesc Calvet. Geologica Acta: an international earth science journal, 2, 257–269.

Vandeginste, V., John, C. M., 2013. Diagenetic implications of stylolitization in pelagic carbonates, Canterbury Basin, offshore New Zealand. Journal of Sedimentary Research, 83, 226–240.

ACCEPTED MANUSCRIPT

Vandeginste, V., Swennen, R., Gleeson, S. A., Ellam, R. M., Osadetz, K., Roure, F. 2009. Thermochemical sulphate reduction in the Upper Devonian Cairn Formation of the Fairholme carbonate complex (South- West Alberta, Canadian Rockies): evidence from fluid inclusions and isotopic data. Sedimentology, 56, 439–460.

Veizer, J., Ala, D., Azmy, K., Bruckschen, P., Buhl, D., Bruhn, F., Garden, G. A. F., Diener, A., Ebneth, S., Godderis, Y., Jasper, T., Korte, C., Pawellek, F., Podlaha, O. G. Strauss, H., 1999. $^{87}Sr/^{86}Sr$, $\delta^{13}C$ and $\delta^{18}O$ evolution of Phanerozoic seawater. Chemical Geology, 161, 59–88.

Volery, C., Davaud, E., Foubert, A., Caline, B., 2010. Lacustrine microporous micrites of the Madrid Basin (Late Miocene, Spain) as analogues for shallow-marine carbonates of the Mishrif reservoir Formation (Cenomanian to Early Turonian, Middle East). Facies, 56, 385–397.

Worden, R. H., Smalley, P. C., Cross, M. M., 2000. The influence of rock fabric and mineralogy on thermochemical sulfate reduction: Khuff Formation, Abu Dhabi. Journal of Sedimentary Research, 70, 1210–1221.

Zeeh, S., Bechstädt, T., McKenzie, J., Richter, D. K., 1995. Diagenetic evolution of the Carnian Wetterstein platforms of the Eastern Alps. Sedimentology, 42, 199–222.

ACCEPTED MANUSCRIPT

Ziegler, M. A., 2001. Late Permian to Holocene paleofacies evolution of the Arabian Plate and its hydrocarbon occurrences. GeoArabia, 6, 445–504.

ACCEPTED MANUSCRIPT

ACCEPTED MANUSCRIPT

Figure Captions

Figure 1. (A) Small-scale map of the Arabian Peninsula. (B) Location of the field based on a paleofacies map of the Late Jurassic during the deposition of the Arab and Hith formations (modified after Ziegler, 2001). (C) Map of the studied anticline showing the location of the studied wells in the crest (A, B and C) and flank (D).

Figure 2. A simplified stratigraphic column of the Upper Jurassic in the study area, showing the various members of the Arab Formation and the Hith Formation.

Figure 3. Optical photomicrographs (PPL) of various diagenetic phases in the upper Arab D Member. (A) Grainstone with completely micritized ooids displaying varying microporosity (blue epoxy; crest). (B) Grainstone with completely micritized ooids and no visible microporosity (flank). (C) Grainstone with micritized ooids, intraclasts and bioclasts that is partly calcite cemented and showing relatively high intergranular volume (crest). (D) Grainstone with dominantly non- to partly micritized ooids showing low intergranular volume (crest). Cement is mainly present inside and in the vicinity of allochems that have been dissolved (arrows). Allochems are severely compacted where cement is absent (red arrow). (E) Grainstone with micritized ooids and bioclasts, cemented by mainly fine to medium equant calcite showing relatively high intergranular volume (flank). (F)

ACCEPTED MANUSCRIPT

Grainstone with dominantly non-micritized ooids that is severely compacted (flank). (G) Grainstone with an almost completely dissolved micritized grain. Various amounts of micrite is common in party dissolved grains (arrow; crest). (H) Grainstone with grains showing varying degree of micritization. Micritized parts of the grains (yellow arrows) have more microporosity than non-micritized grains (red arrows). Note that intergranular volume is relatively high where equant calcite cement is present (blue arrows).

Figure 4. SEM images of peloids in the upper Arab D Member. (A) Peloid in the crest. (B) Peloid in the flank. (C) Higher magnification image of pleoid with microporosity in the crest (D) Higher magnification image of nearly completely cemented micropores in a peloid from the flank.

Figure 5. Optical and CL photomicrographs of grainstones in the crest. (A) and (B) Dull orange luminescent intergranular fine to medium equant (yellow arrow) and intragranular dull orange to yellow luminescence drusy (red arrow) calcite cements. Saddle dolomite cement is bright red luminescent. (C) and (D) Dull orange luminescent fine to medium equant (red arrow) calcite cements. Saddle dolomite cement has bright red CL colors (red arrow).

Figure 6. Optical photomicrographs showing: (A) Syntaxial calcite overgrowth around echinoderm fragment (PPL; crest; upper Arab D). Note the high and low intergranular volume

ACCEPTED MANUSCRIPT

between the peloids where syntaxial calcite cement is present (yellow arrows) and absent (red arrow), respectively. (B) Micritized grainstone with abundant fine to medium equant calcite (red arrow) and drusy calcite (yellow arrows) cements in intergranular and moldic pores (PPL; flank; upper Arab D). Quartz cement has partly replaced a bioclast (blue arrow). (C) Celestine cement (yellow arrow) and anhydrite nodule (red arrow) that have replaced host limestone (XPL; crest; lower Arab D). (D) Calcite (stained pink) and saddle dolomite (unstained) that have replaced anhydrite (PPL; flank; lower Arab D). Small relicts of anhydrite is commonly observed in the calcite (arrows). (E) Low-amplitude stylolite with minor carbonate cements (PPL; crest; lower Arab D). (F) Microfractures associated with a stylolite are filled by fine to medium equant calcite cement (yellow arrow). Saddle dolomite is observed along the stylolite (blue arrow; PPL; flank; lower Arab D). (G) Floatstone with saddle dolomite in fractures and moldic pores (PPL; crest; lower Arab D). (H) Blocky calcite cement engulfing and partly replacing saddle dolomite (arrows) along a stylolite (PPL; flank; lower Arab D).

Figure 7. Cross-plot of carbon *versus* oxygen isotope composition of various carbonates. The blue rectangle represents the isotope composition of calcites precipitated in equilibrium with Kimmeridgian to Tithonian seawater (Veizer et al., 1999). Note that the majority of the carbonates analyzed

ACCEPTED MANUSCRIPT

have similar $\delta^{13}C_{VPDB}$ values as Kimmeridgian to Tithonian seawater.

Figure 8. Cross-plot of $^{87}Sr/^{86}Sr$ ratios *versus* oxygen isotope composition of various generations of calcite and saddle dolomite. Note that all carbonates analyzed show similar $^{87}Sr/^{86}Sr$ ratios as those inferred for Kimmeridgian to Tithonian seawater (Veizer et al., 1999).

Figure 9. Optical photomicrographs showing: (A) and (B) Primary fluid inclusion assemblages within blocky calcite crystals (flank; outer ramp). (C) and (D) Fluid inclusions in saddle dolomite concentrated in crystal cores (blue arrows; flank; outer ramp).

Figure 10. Frequency distribution (blue = crest; red = flank) of homogenization temperatures (T_h) for: (A) Fine to medium equant calcite cements in the upper Arab D Member. (B) Drusy calcite cements in the upper Arab D Member. (C) Syntaxial calcite overgrowths from the crest and flank in the upper Arab D Member. (D) Celestine cement from crest in the lower Arab D Member. (E) Blocky calcite cement from the crest and flank in the lower Arab D Member. (F) Saddle dolomite from crest and flank in the lower Arab D Member, which has the highest T_h of all phases in the Arab Formation. (G) Cross-plot of total salinity *versus* T_h in blocky calcite and saddle dolomite cements from the flank.

ACCEPTED MANUSCRIPT

ACCEPTED MANUSCRIPT

Figure 11. Burial history curve for the studied crest and flank wells in the Arab Formation spanning from deposition to present time (modified after Al Darmaki et al., 2014).

Figure 12. The paragenetic sequence constructed for the Arab Formation in relation to burial and tectonic events (? = uncertain event). Stylolitization during obduction of Oman Ophiolites and Zagros Orogeny is inferred to result in minor tectonic stylolites. The diagenetic phases and events after gas emplacement affected mainly the flanks. After the obduction, the temperature in the crest and flank was around 90°C and 115°C, respectively. The present day temperature in the crest and flank of the anticline is around 140°C and 160°C, respectively.

Figure 13. Schematic illustration of the diagenetic and reservoir quality evolution in grainstones during: (A) near-surface to burial diagenesis; and (B) the obduction of Oman ophiolites and subsequent subsidence. The porosity is suggested to be completely destroyed in the flanks owing to more severe stylolitization and be preserved in the crest due to gas emplacement.

ACCEPTED MANUSCRIPT

ACCEPTED MANUSCRIPT

Member	***Upper Arab D***					***Lower Arab D***			
	Bulk	Macroporosity	Equant calcite (C2)	Drusy calcite (C3)	Syntaxial calcite (C4)	Bulk	Burial sulfates	Blocky calcite (C5)	Saddle dolomite
Crest									
Thin sections	64					89			
Quantity (%)		0–11	C2+C3[a] = 14–52		1–7		0–25	0–27	0–11
Av.		3.5	27		3		6	13	5.5
n		27	27		27		13	13	13
$\delta^{13}C$ (‰)	–3.0/+2.2				–1.2/+1.7	+1.6/+2.5		+1.1/+2.0	+0.4/+2.0
Av.	+1.2				+0.5	+2.2		+1.7	+1.2
n	15				3	17		4	4
$\delta^{18}O$ (‰)	–5.5/–3.6				–7.2/–5.2	–5.8/–3.7		–6.5/–4.7	–7.7/–3.7
Av.	–5.1				–6.2	–5.0		–6.0	–5.7
n	15				3	17		4	4
T_h (°C)				65–125	80–125		100–120	120–130	140–160
Mode				95	95		110	125	155
n				38	18		18	24	9
Stylolites	20 – 0.19/ft					132 –1.07/ft			
Flank									
Thin sections	24					63			
Quantity (%)		0	C2+C3[a] = 18–46		2–7		0	0–29	0–14
Av.		0	35		3.5		0	19	6.5
n		10	10		10		7	7	7
$\delta^{13}C$ (‰)	+1.0/+3.6					+1.1/+3.3		+0.6/+2.1	+1.9/+3.6
Av.	+1.6					+2.1		+1.5	+2.8
n	7					16		4	4
$\delta^{18}O$ (‰)	–5.9/–3.8					–6.6/–2.9		–5.0/–4.1	–4.2/–2.9
Av.	–4.7					–5.0		–4.6	–3.6
n	7					16		4	4
T_h (°C)			55–130		80–120			115–160	145–175
Mode			90		105/110			145	160
n			62		12			40	47
Salinity (wt%)								19.2–25.2	25.6–26.3
n								27	6
Stylolites	51 – 0.82/ft					247 –1.36/ft			
Suggested main source			Dissolved micrite/stylolitization	Dissolved micrite/stylolitization	Dissolved micrite/stylolitization		Dissolved anhydrite in Arab A–C	Basinal brines/TSR	Basinal brines

Table 1. Summary of the point counting, isotope and fluid inclusion microthermometry results.

[a] Equant and drusy calcite cements were difficult to separate during point counting and they have hence been placed in the same group of cement.

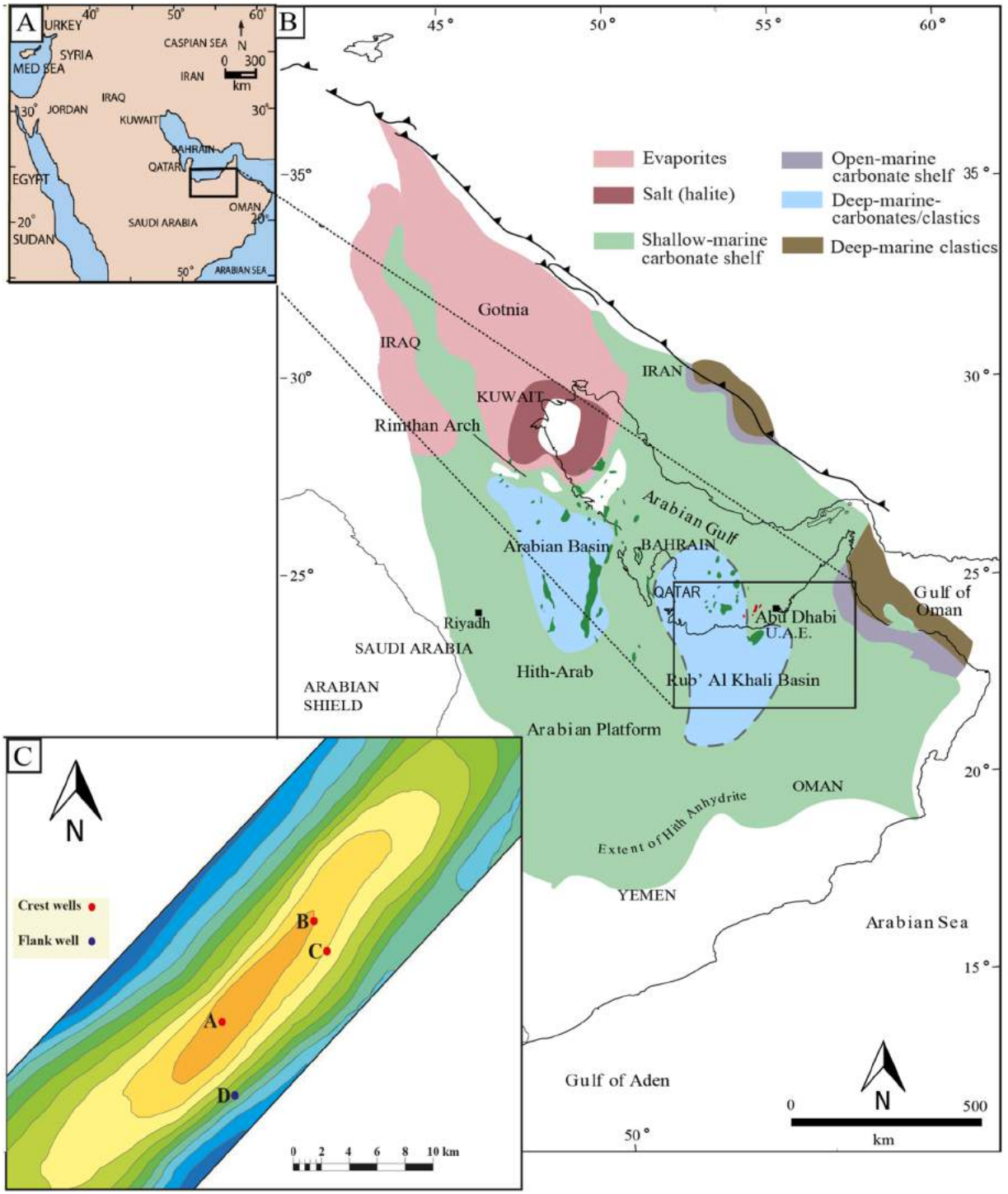
A
TURKEY
SYRIA
MED SEA
CASPIAN SEA
IRAN
IRAQ
JORDAN
KUWAIT
BAHRAIN
QATAR
EGYPT
OMAN
SAUDI ARABIA
SUDAN
ARABIAN SEA
N
0 300
km
B
Evaporites
Salt (halite)
Shallow-marine carbonate shelf
Open-marine carbonate shelf
Deep-marine-carbonates/clastics
Deep-marine clastics
Gotnia
IRAQ
IRAN
KUWAIT
Rimthan Arch
Arabian Gulf
Arabian Basin
BAHRAIN
QATAR
Abu Dhabi
U.A.E.
Gulf of Oman
Riyadh
SAUDI ARABIA
Hith-Arab
Rub' Al Khali Basin
ARABIAN SHIELD
Arabian Platform
OMAN
Extent of Hith Anhydrite
YEMEN
Arabian Sea
Gulf of Aden
45°
50°
55°
60°
35°
30°
25°
20°
15°
0 N 500
km
C
N
Crest wells
Flank well
A
B
C
D
0 2 4 6 8 10 km

Figure 1

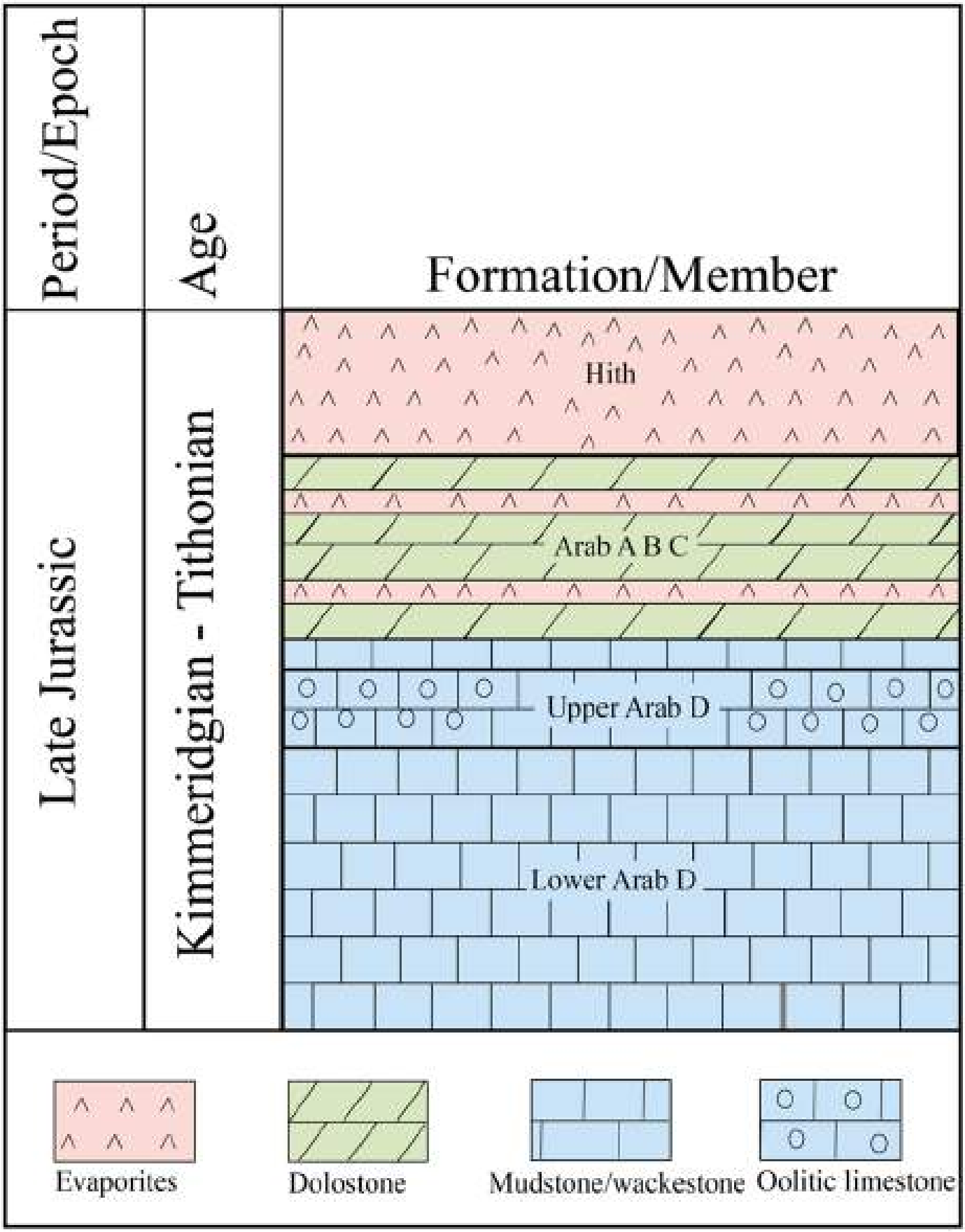
Period/Epoch
Age
Formation/Member
Late Jurassic
Kimmeridgian - Tithonian
Hith
Arab A B C
Upper Arab D
Lower Arab D
Evaporites
Dolostone
Mudstone/wackestone
Oolitic limestone

Figure 2

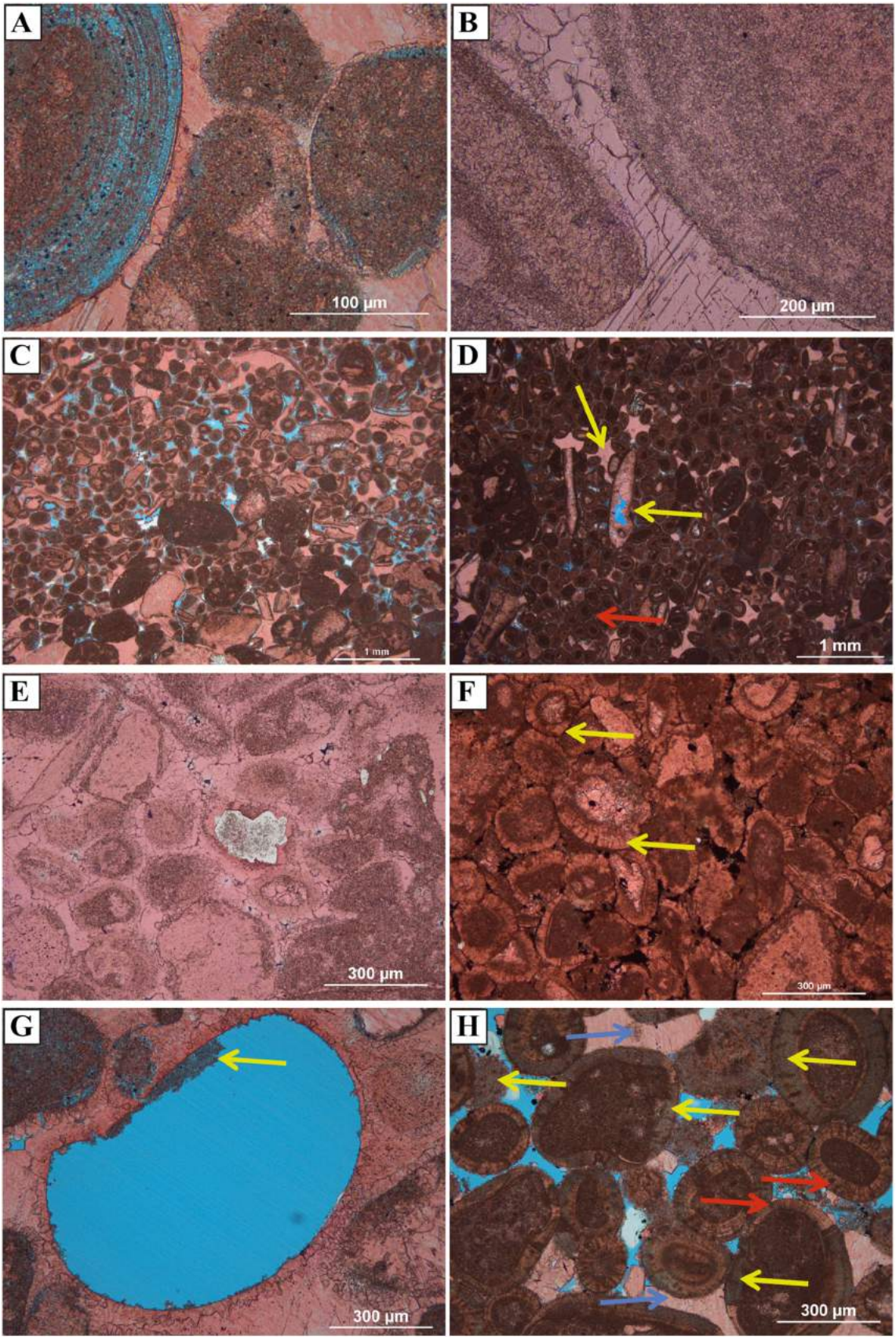

Figure 3

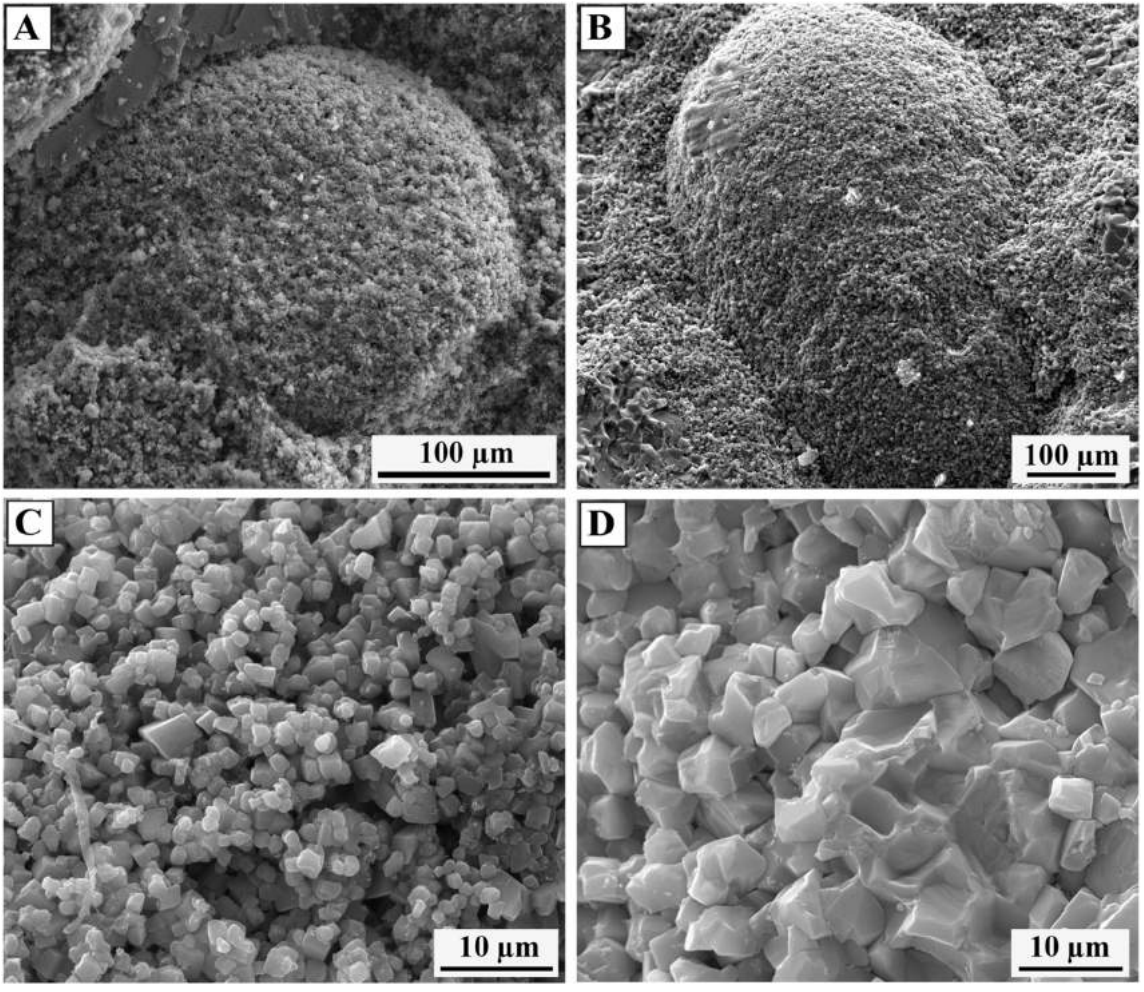

Figure 4

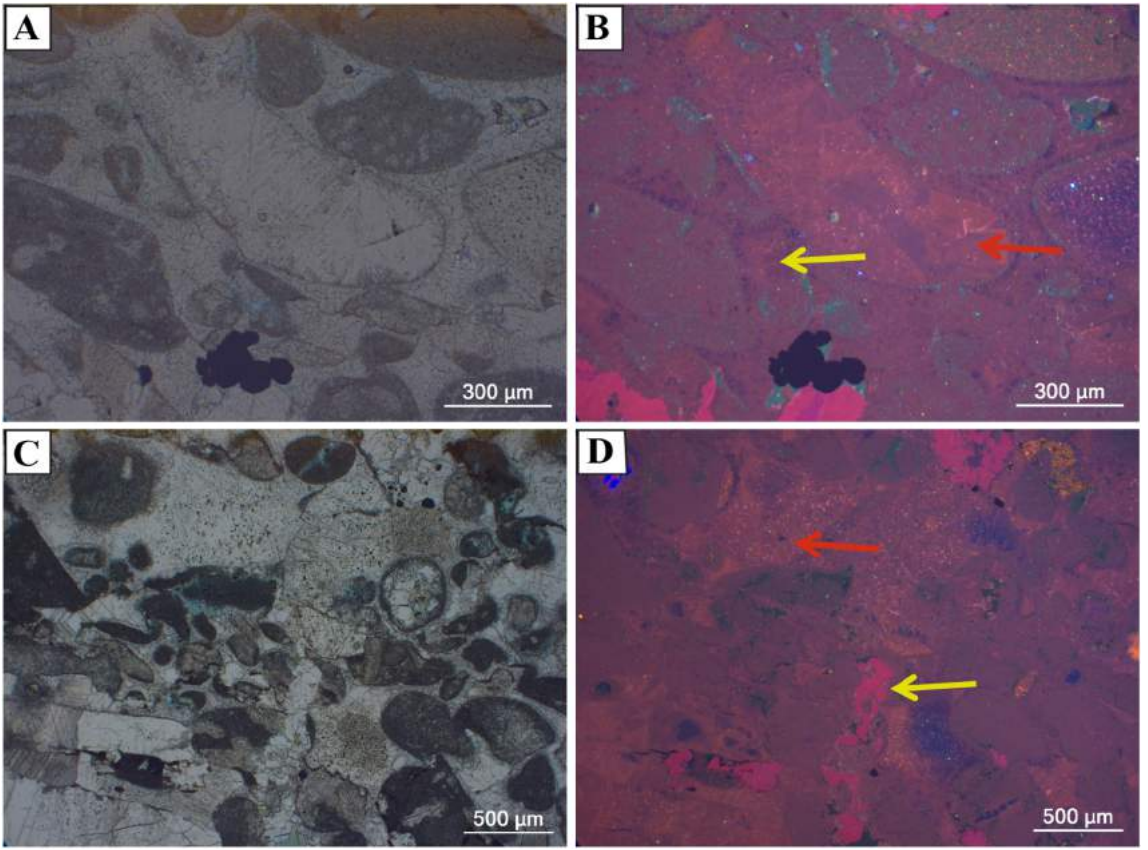

Figure 5

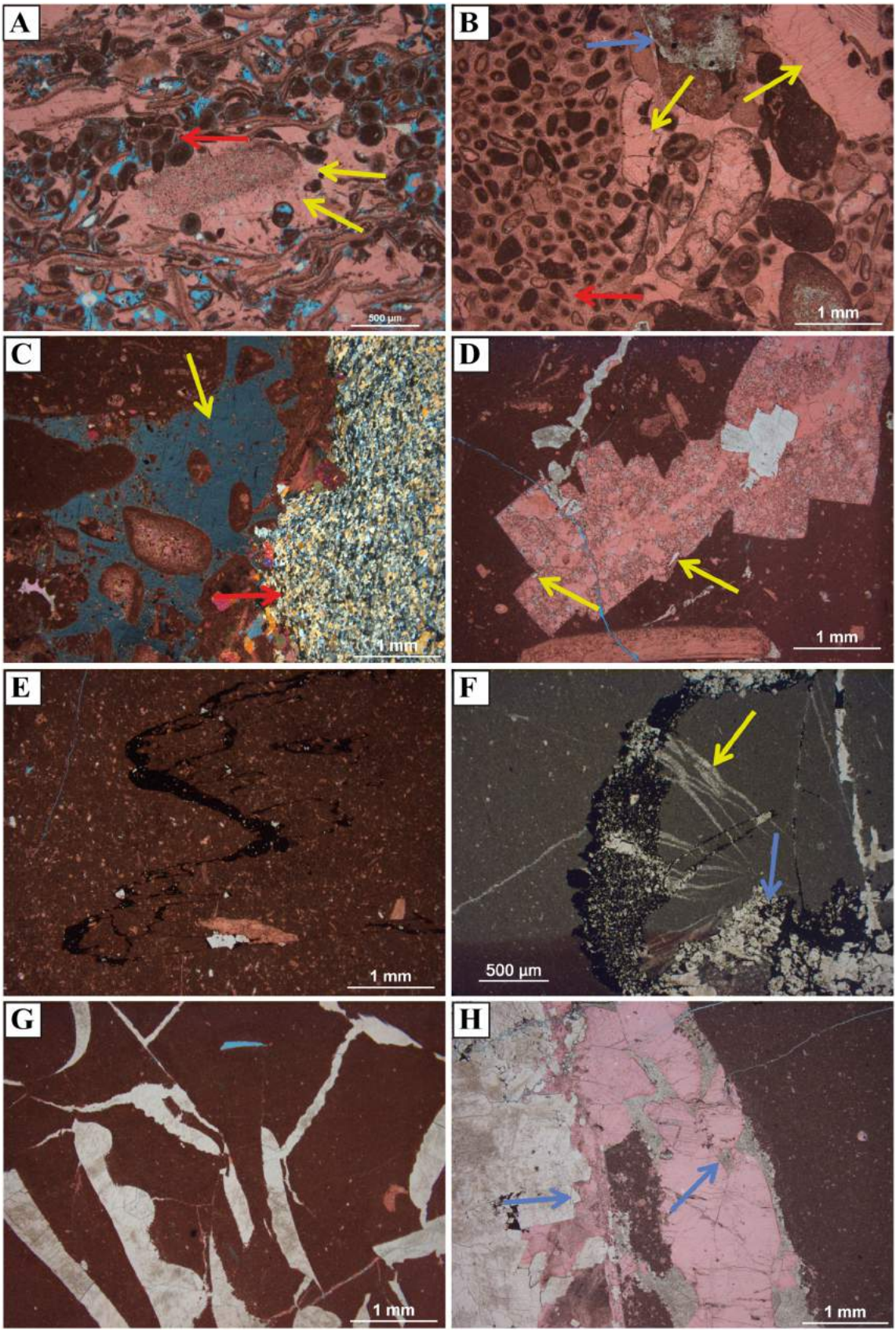

Figure 6

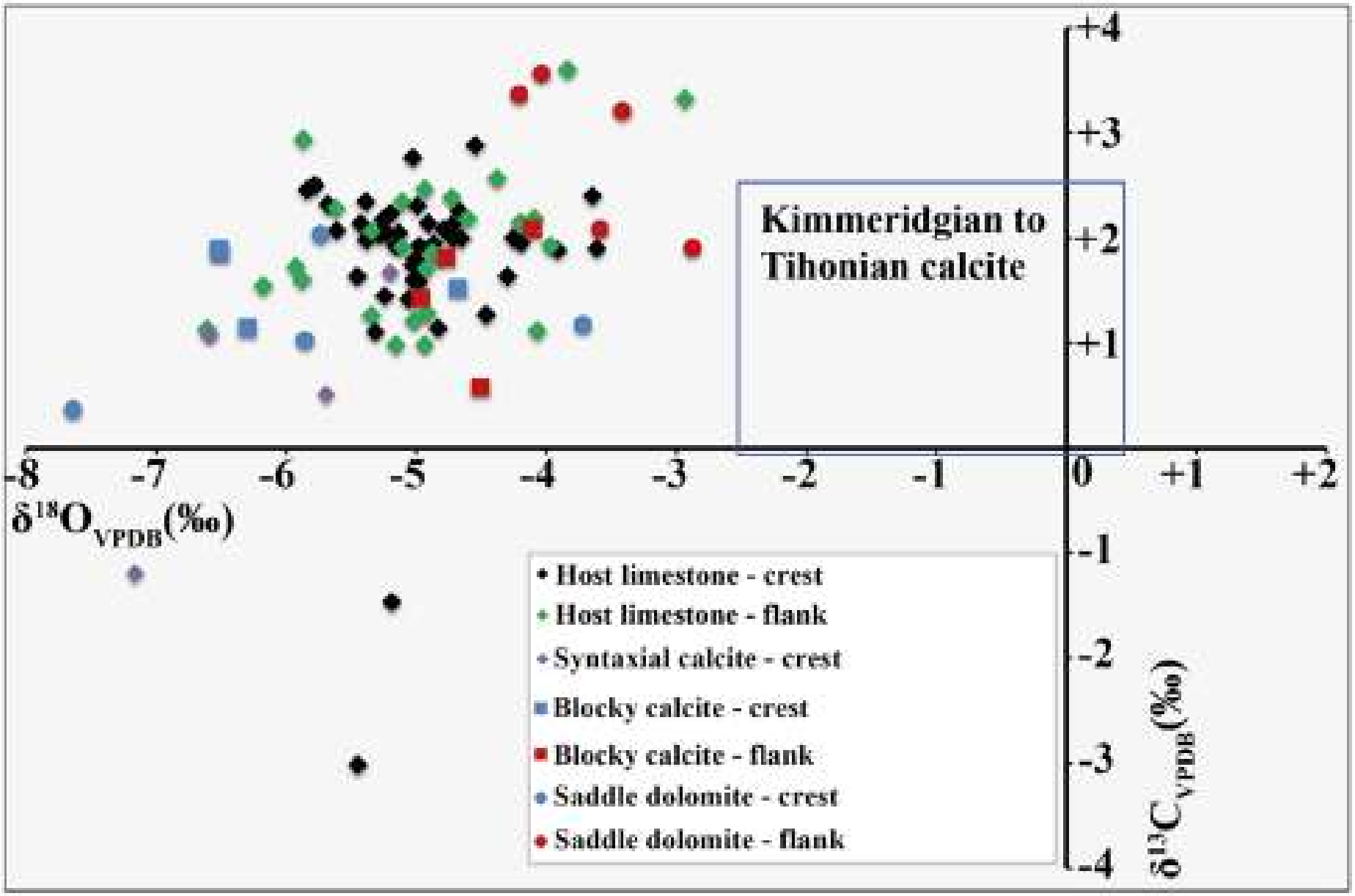
Kimmeridgian to Tithonian calcite
Host limestone - crest
Host limestone - flank
Syntaxial calcite - crest
Blocky calcite - crest
Blocky calcite - flank
Saddle dolomite - crest
Saddle dolomite - flank
δ18OVPDB(‰)
δ13CVPDB(‰)
-8
-7
-6
-5
-4
-3
-2
-1
0
+1
+2
+4
+3
+2
+1
-1
-2
-3
-4

Figure 7

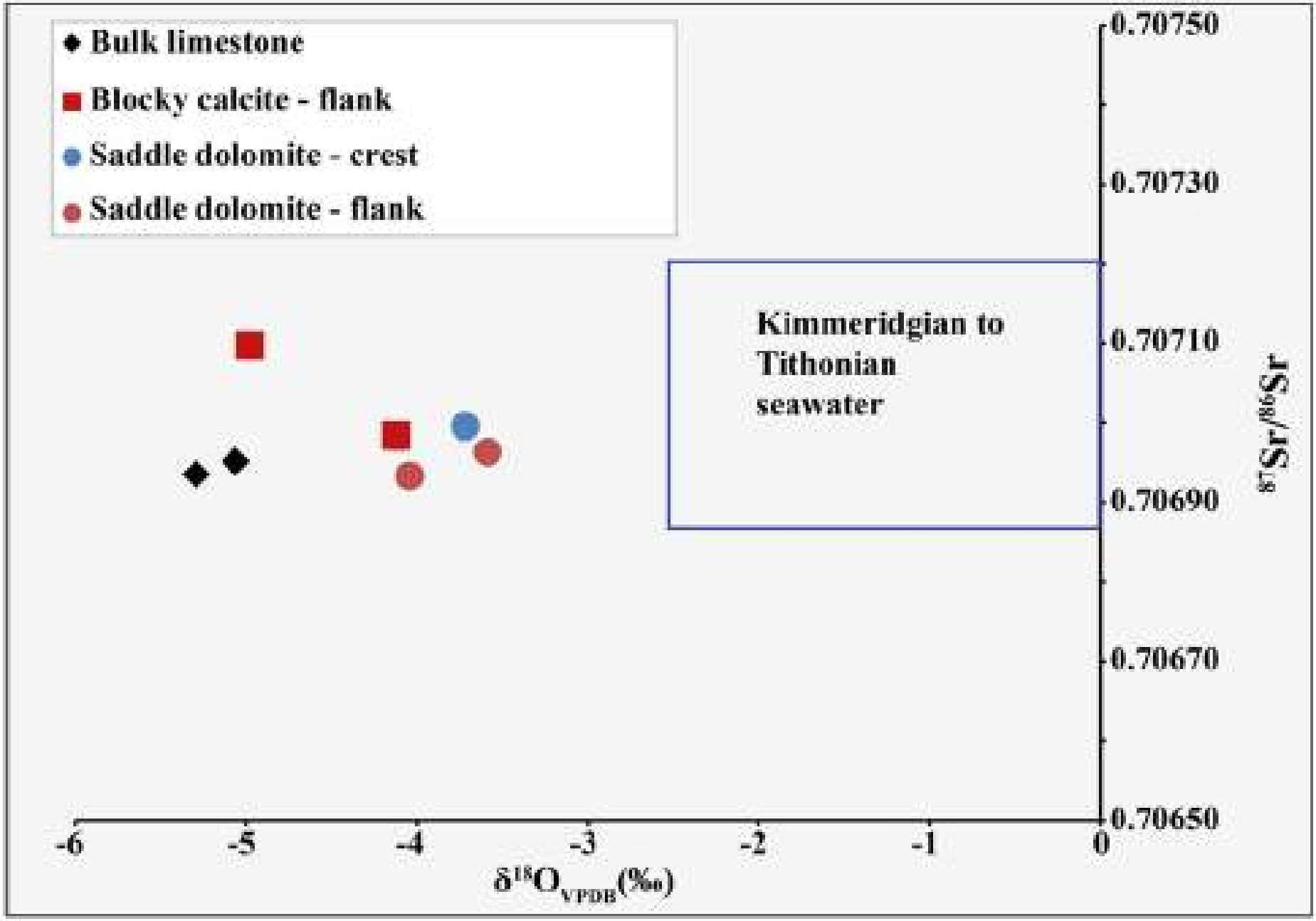
Bulk limestone
Blocky calcite - flank
Saddle dolomite - crest
Saddle dolomite - flank
Kimmeridgian to Tithonian seawater
0.70750
0.70730
0.70710
0.70690
0.70670
0.70650
$^{87}Sr/^{86}Sr$
-6
-5
-4
-3
-2
-1
0
$\delta^{18}O_{VPDB}$(‰)

Figure 8

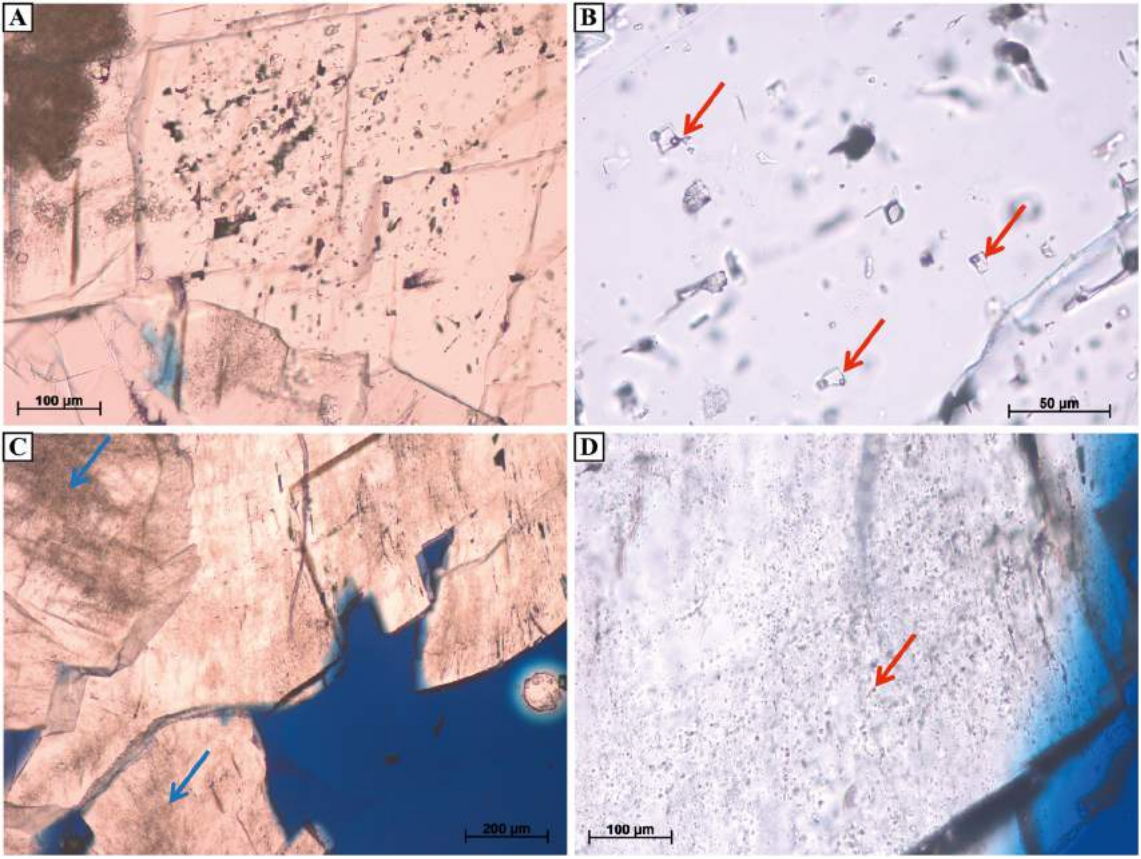

Figure 9

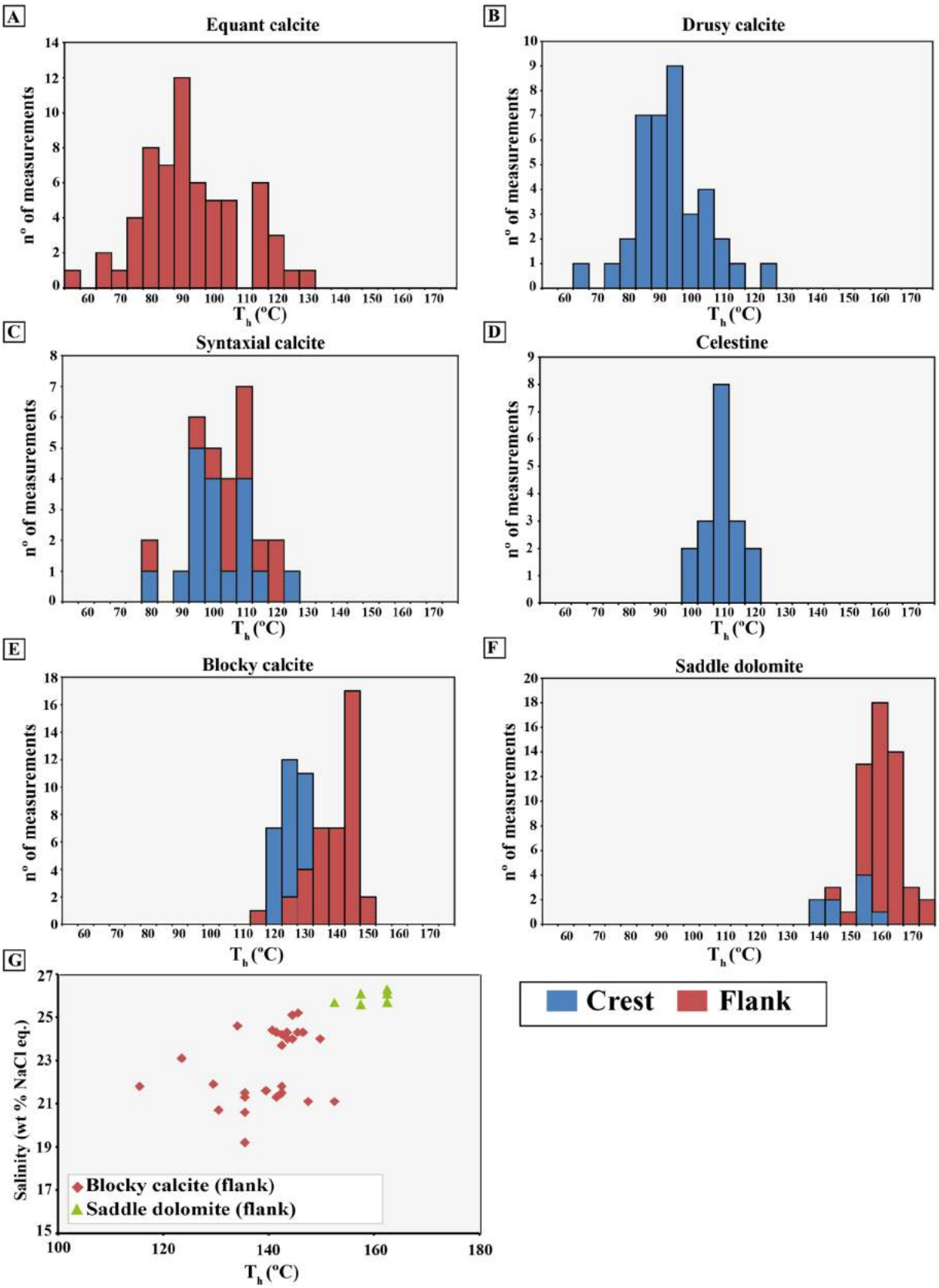
A
Equant calcite
n° of measurements
T$_h$ (°C)
B
Drusy calcite
n° of measurements
T$_h$ (°C)
C
Syntaxial calcite
n° of measurements
T$_h$ (°C)
D
Celestine
n° of measurements
T$_h$ (°C)
E
Blocky calcite
n° of measurements
T$_h$ (°C)
F
Saddle dolomite
n° of measurements
T$_h$ (°C)
Crest
Flank
G
Salinity (wt % NaCl eq.)
Blocky calcite (flank)
Saddle dolomite (flank)
T$_h$ (°C)

Figure 10

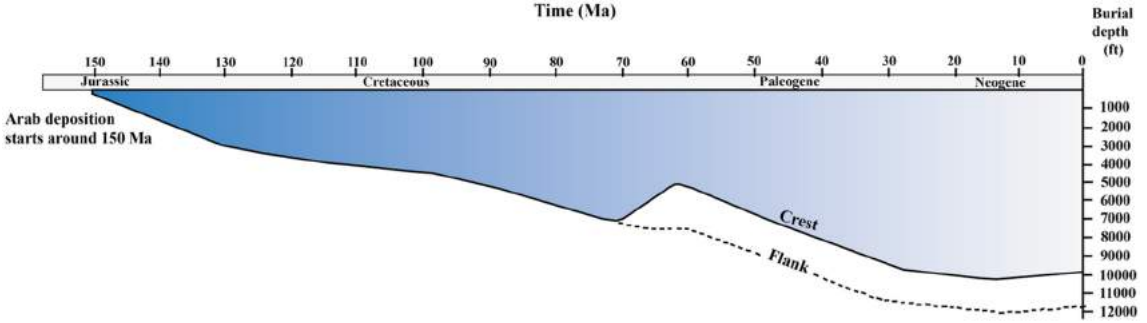
Time (Ma)
Burial depth (ft)
150
140
130
120
110
100
90
80
70
60
50
40
30
20
10
0
Jurassic
Cretaceous
Paleogene
Neogene
Arab deposition starts around 150 Ma
1000
2000
3000
4000
5000
6000
7000
8000
9000
10000
11000
12000
Crest
Flank

Figure 11

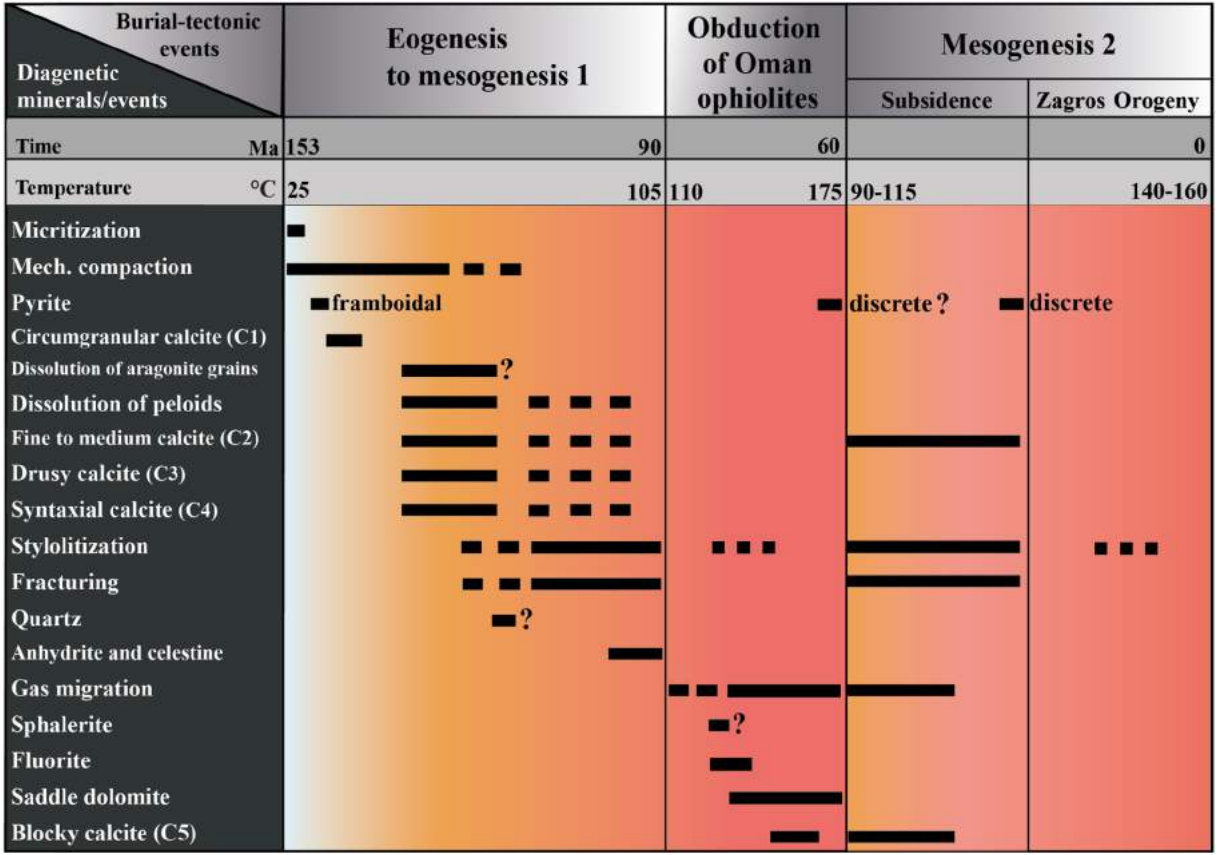
Burial-tectonic events
Diagenetic minerals/events
Eogenesis to mesogenesis 1
Obduction of Oman ophiolites
Mesogenesis 2
Subsidence
Zagros Orogeny
Time Ma
153
90
60
0
Temperature °C
25
105
110
175
90-115
140-160
Micritization
Mech. compaction
Pyrite
framboidal
discrete ?
discrete
Circumgranular calcite (C1)
Dissolution of aragonite grains
?
Dissolution of peloids
Fine to medium calcite (C2)
Drusy calcite (C3)
Syntaxial calcite (C4)
Stylolitization
Fracturing
Quartz
?
Anhydrite and celestine
Gas migration
Sphalerite
?
Fluorite
Saddle dolomite
Blocky calcite (C5)

Figure 12

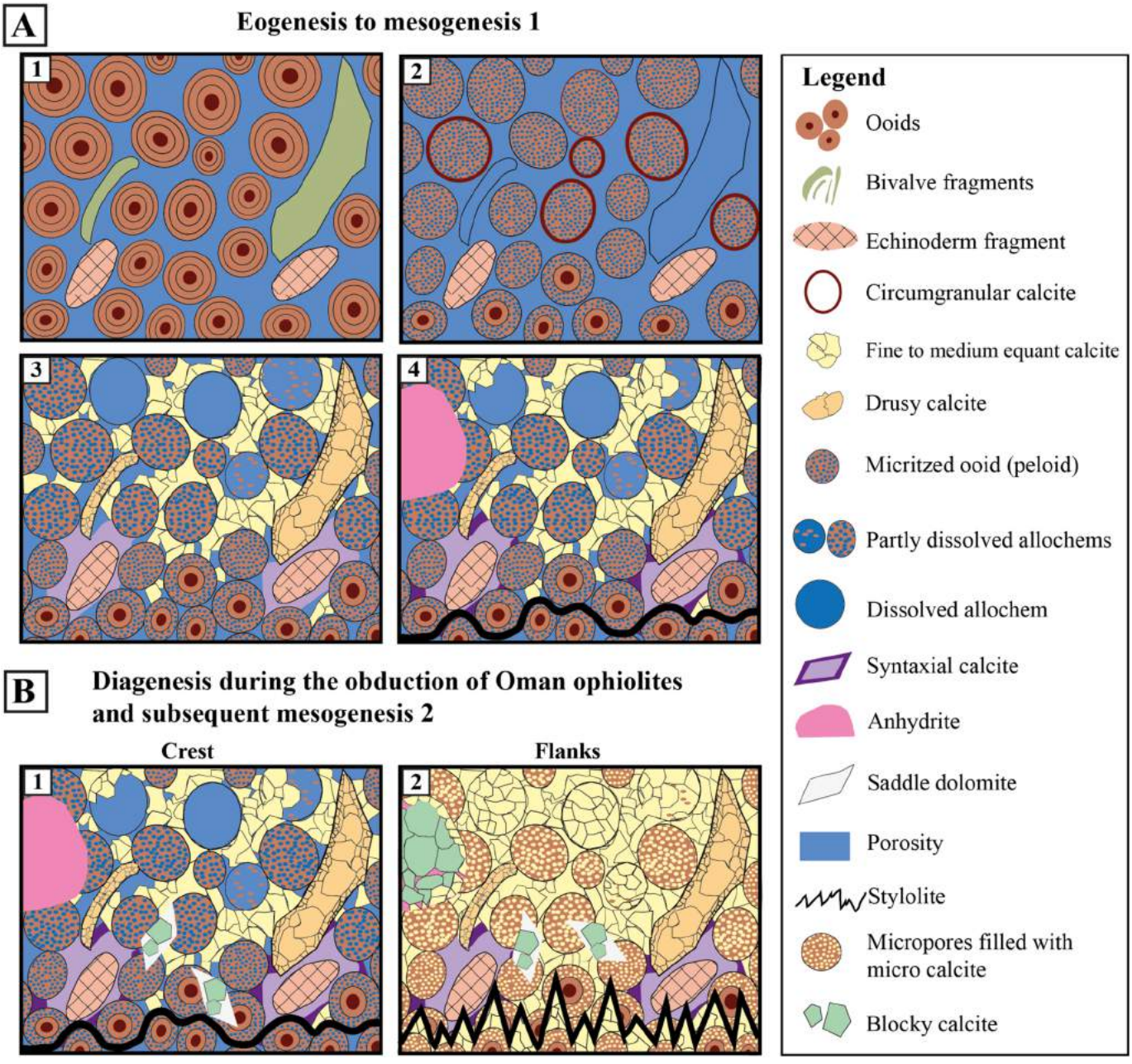
A
Eogenesis to mesogenesis 1
1
2
3
4
B
Diagenesis during the obduction of Oman ophiolites and subsequent mesogenesis 2
Crest
Flanks
1
2
Legend
Ooids
Bivalve fragments
Echinoderm fragment
Circumgranular calcite
Fine to medium equant calcite
Drusy calcite
Micritzed ooid (peloid)
Partly dissolved allochems
Dissolved allochem
Syntaxial calcite
Anhydrite
Saddle dolomite
Porosity
Stylolite
Micropores filled with micro calcite
Blocky calcite

Figure 13